Chemical Engineering Journal 439 (2022) 135542

Contents lists available at ScienceDirect

Chemical Engineering Journal

journal homepage: www.elsevier.com/locate/cej

Silver metal organic frameworks and copper metal organic frameworks immobilized on graphene oxide for enhanced adsorption in water treatment

Medha Kasula, Tin Le, Adrienne Thomsen, Milad Rabbani Esfahani *

Department of Chemical and Biological Engineering, University of Alabama, Tuscaloosa, United States

ARTICLE INFO

Keywords:
Metal-organic framework
Water treatment
Wastewater treatment
Dye adsorption
Graphene-oxide
Langmuir
Freundlich
Temkin

ABSTRACT

In this study, copper metal organic frameworks (Cu-MOF) and silver metal organic frameworks (Ag-MOF) were synthesized and immobilized on and between GO sheets using an ultrasonication process. The GO-immobilized MOFs (GO-Ag-MOF and GO-Cu-MOF) showed enhanced physicochemical properties, including enhanced surface area, surface charge, and active adsorption sites confirmed with characterization techniques such as zeta potential, Brunauer–Emmett–Teller (BET), X-ray diffraction (XRD) and scanning electron microscopy (SEM). In addition, the adsorption capacities of Ag-MOF, Cu-MOF, GO-Ag-MOF, and GO-Cu-MOF materials for methylene blue dye (MB), as an organic contaminant model, were thoroughly evaluated at different experimental conditions (pH (3–10), temperature (25–45 °C), and adsorbate concentrations (0–150 ppm)). The kinetics and thermodynamic behavior of the synthesized MOFs revealed that both GO-Ag-MOF and GO-Cu-MOF showed around 10% increase in adsorption capacity in comparison to the pristine Ag-MOF and Cu-MOF at all the tested conditions. GO-Ag-MOF exhibited more than 98 % dye removal, followed by Ag-MOF (90%), GO-Cu-MOF (75%), and Cu-MOF (65%). The main mechanism for adsorption was monolayer adsorption based on electrostatic interactions. All MOFs showed more than 80% re-generability after three regeneration cycles

1. Introduction

Metal-Organic Frameworks (MOF) are 3D crystalline materials with a highly porous structure introduced recently as the new generation of adsorbents.[1–4] The synergistic connection between the metallic atom and an organic ligand by coordination gives MOFs' the flexibility to act as adsorbents for sulfur compounds[5], phenols[6], dyes[7], and pharmaceutical products.[8] MOFs' unique characteristics, such as selectivity, enhanced surface area, shape tunability, pore size, and porosity, accentuate their application in removing different types of contaminants from wastewater.[9–12] The morphological and physicochemical properties of MOFs play a critical role in the adsorption process. For instance, MOF pore size, geometry, hydrogen bonding, π-π bond interactions, acid-base interactions, and electrostatic interactions govern the adsorption process. [13–15]. Cu-BTC MOF, also known as HKUST-1, is one of the most commonly used MOFs in separations, drug delivery, and catalysis due to their exceptional thermal and mechanical stability. [16,17] Wang et al. [18] reported copper-based MOF (JLU-MOF51) had a significant adsorption capacity of greater than 90% for fluorescein disodium, with almost total adsorption occurring after 30 min. Comparatively, other dyes such as MO, rhodamine B, and orange G showed marginal adsorption (<40%) even after 90 min. As such, the authors concluded that the size and shape of the adsorbent and dyes governed the size-selective mechanism of JLU-MOF 51.[18] The same mechanism for MIL-53(Al)–NH_2, along with the hydrogen bonding between the dye and MOF, demonstrated the importance of physicochemical interactions for adsorption.[19] Combined with the intrinsic properties of copper, an exploration into the adsorption properties of copper-composite nanoparticles has shown favorable results in the removal of dye from contaminated wastewater [20]. Ag nanoparticles (NPs) were reported as an effective adsorbent for dyes. Satapathy et al. [21] reported the use of Ag NPs for the removal of crystal violet dye with a high removal efficiency of 97.2% [21,22]. 93 % removal of Rhodamine B dye using biosynthesized AgNPs was reported by Azeez et al. [22]. AgNPs coated onto activated carbon were reported as an efficient adsorbent for a number of dyes [23,24]. However, the use of Ag-MOF for dye removal has not been reported based on our literature review.

One of the critical factors governing MOFs physicochemical properties is the synthesis process. Most of the MOFs have been traditionally synthesized using a solvothermal process. Although there are benefits to

* Corresponding author.
E-mail address: mesfahani@eng.ua.edu (M. Rabbani Esfahani).

https://doi.org/10.1016/j.cej.2022.135542
Received 20 December 2021; Received in revised form 24 February 2022; Accepted 26 February 2022
Available online 3 March 2022

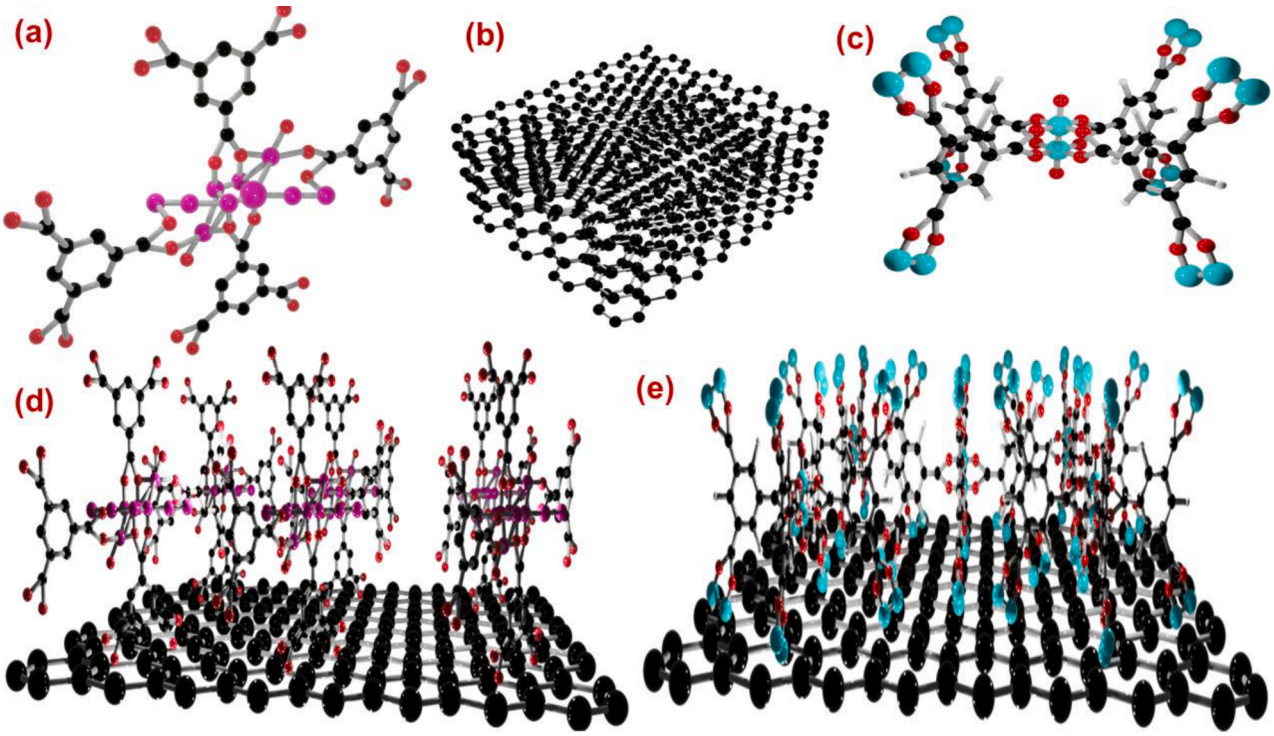

Fig. 1. The molecular schematic of synthesized (a) Ag-MOF, (b) GO sheets, (c) Cu-MOF, (d) GO-Ag-MOF, and (e) GO-Cu-MOF. Black represents carbon, red represents oxygen, white represents hydrogen, purple represents silver atoms, and the cyan color represents copper atoms. (For interpretation of the references to color in this figure legend, the reader is referred to the web version of this article.)

using the solvothermal method, such as higher surface area and better stability, it is carried out at higher temperatures (greater than 120 °C), uses harsher non-environmental friendly chemicals, and has longer synthesis time (greater than 12 h).[25] In this project, we use an alternative method to synthesize MOFs using ultrasonication technique at room temperature (25 °C), fast synthesis time (<1h), and non-hazardous solvent (ethanol) without the need of extreme conditions. It was reported by Abbasi et al., [26] that the sonication method decreased the surface area of the Cu-BTC (371 m^2/g) compared to the mechanosynthesis method (1033 m^2/g), although the uptake of guest molecules on MOF synthesized using the sonication method was remarkable.[26] Despite the advantages, the ultrasonication process is still limited by factors such as low stability at high temperatures and humidity, inadequate surface areas, and small pore volumes, all of which hinder the performance of MOFs' in the adsorption process.[9] To overcome these limitations, the functionalization of MOFs with other compounds is adapted to reinforce the MOF properties. Graphene Oxide (GO) has been shown to be an efficient absorbent for different types of dyes across the color spectrum. [27,28] GO exhibits excellent tunability, low purchase costs, a negative surface charge, and active functional groups, such as edge-located carboxyl groups and basal hydroxyl and epoxide groups, which make GO excel in adsorption compared to other adsorbents. [29–31] Based on the unique properties of GO, reinforcement of MOF structure by GO can mitigate the mentioned MOF drawbacks and enhance the adsorption process. The adsorption of dyes on GO, organic nanoparticles and MOFs has previously been studied individually. However, the synergetic effects of GO-MOFs have not been reported.

In this study, Ag-MOF and Cu-MOF were synthesized and immobilized on or between GO sheets by the facile, rapid, and eco-friendly sonication method. The fabricated GO-Cu-MOF and GO-Ag-MOF compounds were characterized using DLS, zeta potential, BET, FTIR, XRD and SEM techniques to identify the new structure of GO-immobilized MOFs. The adsorption kinetics behavior and the mechanisms of the dye (methylene blue) removal, as a contaminant model, for all the fabricated compounds were investigated at different operational conditions and compared with each other to identify the correlations between MOF structure and adsorption mechanisms.

2. Experimental section

2.1. Materials

Ethanol (Purity, 99%), silver nitrate ($AgNO_3$), copper nitrate hemipentahydrate ($Cu(NO_3)_2$. 2.5 (H_2O), 1, 3, 5-benzentricarboxylic acid (BTC) and methylene blue (MB) ($C_{16}H_{18}ClN_3S.H_20$, $\lambda = 665$ nm) were purchased from Merck (Darmstadt, Germany). Graphene-oxide (GO) nano-powder (US1022) with 1.5–5.5 μm diameter and 0.43–1.23 nm thickness were purchased from US Research Nanomaterial, Inc. (Houston, USA).

2.2. Synthesis of GO-Cu-MOF and GO-Ag-MOF Adsorbent

Four different MOF compounds, including GO-Ag-MOF, GO-Cu-MOF, Ag-MOF, and Cu-MOF, were synthesized *using* the sonication technique.[31] To synthesize the GO-Ag-MOF, 0.5 g of silver nitrate and 0.5 g of BTC were mixed with water and ethanol, respectively, in two separate 20 ml clean flasks for 30 min at room temperature. The resulting solutions were added to a 10 ml graphene oxide/partially reduced graphene oxide (GO/rGO) aqueous solution (5 g/L) and bath sonicated for 30 min to get a fully dispersed solution. The final solution was sonicated via an ultrasonic probe under 20 KHz frequency, 0.6 pulse, and 100 W output energy (Cole-Parmer, 750 W Ultrasonic Processor, USA) for another 30 min. The sonicated mixture was then dried at 40 ℃ in a convection oven (Mode, Fisher Scientific, Hampton, USA) for 24 h. The same procedure was carried out for the fabrication of GO-Cu-MOF except for the addition of a copper nitrate solution instead of a silver nitrate solution. For synthesizing Ag-MOF and Cu-MOF NPs, the same sonication technique was used without the addition of GO into the solution. Fig. 1 represents a schematic of Ag-MOF, Cu-MOF, GO sheets, GO-Cu-MOF, and GO-Ag-MOF.

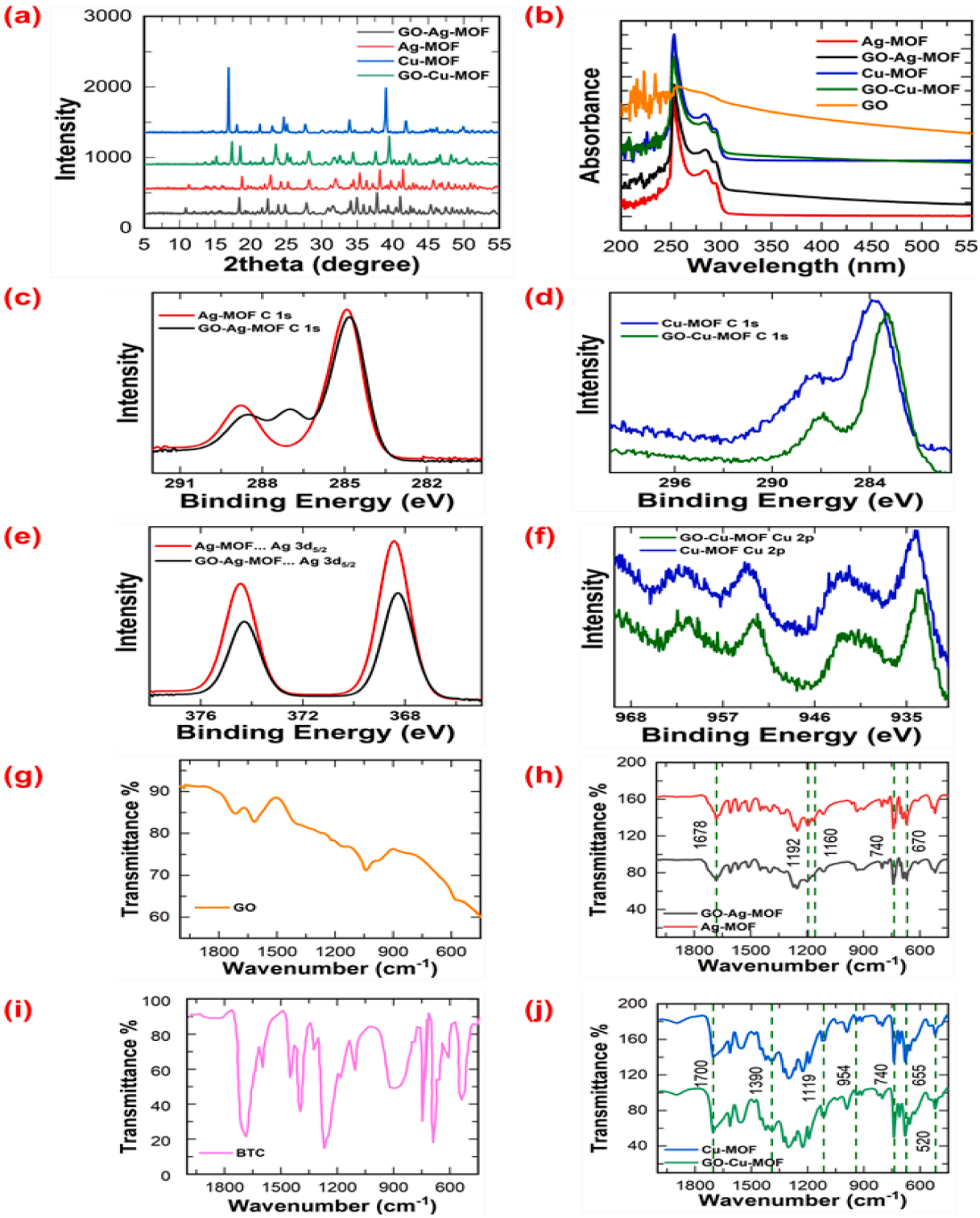

Fig. 2. (a) XRD pattern of Cu-MOF, GO-Cu-MOF, Ag-MOF, and GO-Ag-MOF; (b) UV Vis spectrum of Cu-MOF, GO-Cu-MOF, Ag-MOF, GO-Ag-MOF, GO; (c) The C 1 s spectrum of Ag-MOF and GO-Ag-MOF; (d) The C 1 s spectrum of Cu-MOF, GO-Cu-MOF; (e) The Ag 3d5/2 spectrum of Ag-MOF and GO-Ag-MOF; (f) The Cu 2p spectrum of Cu-MOF and GO-Cu-MOF; The FTIR spectrum of (g) GO (h) Ag-MOF, GO-Ag-MOF, (i) BTC, (j) Cu-MOF, GO-Cu-MOF.

2.3. Characterization Techniques

X-ray powder diffraction (XRD) analysis was performed at 298 K with Co K_α radiation (Bruker D8, Billerica, USA) at theta-2 mode from 5° to 60°. An X-ray photoelectron spectrometer (XPS) (Kratos Axis 165 XPS/ Auger, Shimadzu, Japan) equipped with a 100 μm monochromatic Al K_α X-ray source was used to evaluate the elemental composition of the synthesized MOFs. Brunauer–Emmett–Teller (BET) analysis was performed for the assessment of the pore volume and surface area of the materials using ASAP 2020 (Micromeritics, USA). Zeta potential of the nanoparticles was measured by the Nano ZS Zetasizer (Malvern Panalytical, Malvern, UK). A UV–Vis spectrophotometer (Genesys 10 s, Thermo Fisher, USA) was used for quantifying the MB concentrations at a wavelength of $\lambda = 665$ nm. Thermal stability of the MOFs was tested

using Thermogravimetric and Differential scanning calorimetry (TGA-DSC) (Perkin-Elmer, STA 8000) in a temperature range of 30–500 °C at the heating rate of 10 °C/min under nitrogen atmosphere.

The surface morphology of the nanoparticles was determined using scanning electron microscopy (SEM, JEOL FE 7000, JEOL, Tokyo, Japan) with gold-coated samples. Energy-dispersive X-ray spectroscopy (EDX) (JEOL 7000, JEOL, Tokyo, Japan) was employed for elemental composition and map tracking of the synthesized MOF.

2.4. Adsorption Procedure

Isothermal adsorption studies were conducted at different temperatures (25 and 45 °C), initial dye concentrations (0–150 mg/L), and pH values (3 – 10), with a constant adsorbent concentration of 0.25 g/L. The appropriate amount of dye (adsorbate) solution and synthesized MOF (adsorbent) were added in 40 ml flasks and were shaken on a reciprocating shaker for 24 h at 150 rpm. The temperature of the flasks was controlled by a temperature-controlled water bath. These samples are then centrifuged to separate the MOFs from the dye solution. The pH of the solutions was adjusted using 0.1 M HCl and 0.1 M NaOH. A minimum of three replicates of each solution at the varied experimental conditions were prepared and tested, and an average value was reported. Aliquots for analysis were collected from the solution supernatant. Dye concentration was analyzed using UV–Vis spectroscopy at a wavelength of $\lambda = 665$ nm. The adsorption mechanism was analyzed using Freundlich, Langmuir, and Temkin models.[32–34].

2.5. Regeneration and Reusability

After the complete adsorption cycle, the exhausted MOFs (MOF saturated with MB) were regenerated using 0.01 M NaOH to test the feasibility of regenerating (restoring) the exhausted MOF. The MOFs were separated from the dye solution using 0.05 μm filter (Whatman Schleicher & Schuell). The MOFs were then dispersed in 0.01 M NaOH solution and placed in an ultrasonication bath for 15–20 min and washed with DI water several times to remove dye and NaOH from the solution. The MOFs were then dried overnight in an oven at 40 °C for use in the next adsorption. The same process was repeated for three adsorption–desorption (regeneration) cycles, and the regeneration efficiency was calculated based on the dye removal performance.

3. Result and discussion

3.1. Structural Characteristics

Fig. 2a shows the XRD pattern of all fabricated MOFs. In agreement with the reported data in the literature the peaks at $2\theta = 13.61°$, 15.4°, 17.39°, 18.53°, 21.81°, 23.48°, 25.13°, 28.21°, were confirmed for the Cu-MOF, which were indexed to the lattice indices of (222), (400), (511), (440), (600), (551), (553) and (555).[35,36] The main peaks at 200, 220, 222, 400 are generally related to the crystallinity of Cu-MOF. The presence of peaks at 222 and 400 in Cu-MOF and GO-Cu-MOF corresponds to the successful crystallinity of MOFs. No clear peaks were observed at 200 and 220 located at $2\theta = 6.88°$, 9.35° respectively, which might be due to the different crystalline structures of MOF synthesized using the ultrasonication method instead of the solvothermal method. GO-Cu-MOF XRD consisted of all the diffraction peaks as that in Cu-MOF crystal, suggesting that the crystallinity and the structure of Cu-MOF have remained intact even after the interaction with GO under sonication. A peak at $2\theta = 10°$ and a peak from $2\theta = 20°$ to 30° with a d-spacing of 0.356 nm showed the presence of GO and partially reduced GO. The XRD of GO (Figure S1) after sonication suggests that sonication has increased the d-spacing of GO to d = 0.389 nm and the peak at $2\theta = 10°$ disappeared which is a sign of exfoliation. [37 38] For the Ag-MOF and GO-Ag-MOF peaks at $2\theta = 39.2°$ and 45° are attributed to the silver nanoparticles face center cubic planes (111) and (200). The XRD pattern of Ag-MOF and Cu-MOF were similar to GO-Ag-MOF and GO-Cu-MOF, respectively, with no peak at 2theta = 10 that suggests Ag-MOF and Cu-MOF were successfully synthesized in the presence of exfoliated GO in agreement with that reported in the literature.[39].

In order to probe the binding mechanism between MOFs and partially rGO, the composite material was further characterized by UV − vis spectroscopy (Fig. 2b). rGO sonicated in water exhibited a broad absorption peak at 258 nm and a weak shoulder peak at about 300 nm as shown in SI (Figure S2), which could be assigned to $\pi \rightarrow \pi^*$ transitions of unoxidized aromatic C–C bonds and $n \rightarrow \pi^*$ transitions of C-O bonds, respectively. [40,41] The UV–vis spectrum of GO-Cu-MOF revealed three peaks around 254, 283, and 290 nm, corresponding to the electronic transition of aromatic rings, $\pi \rightarrow \pi^*$ and $n \rightarrow \pi^*$ transitions of C═O bonds, respectively. The absorption peak of GO at 258 nm was shifted to 254 nm for the solution of GO-Cu-MOF, which is likely due to the π electrons coupling between the linker in the MOF framework and the unoxidized aromatic rings. [42,43] Similar patterns were observed for Ag-MOF and GO-Ag-MOF UV–vis, which might suggest that the structure of Ag-MOF might be similar to Cu-MOF. The UV–Vis spectrum of BTC also showed a typical peak around 254 nm.[44] Ag-MOF and Cu-MOF showed the same UV–Vis pattern similar to the BTC spectrum as BTC forms their main structure. The GO-Ag-MOF and GO-Cu-MOF showed similar peaks as BTC, which indicates that both Ag-MOF and Cu-MOF were located on the GO sheet and covered GO surface.

The XPS spectra of Ag-MOF and GO-Ag-MOF NPs (Fig. 2c) shows the non-oxygenated carbon peak (C–C, and C = C) and oxygenated carbon peak (C-O, and C = O) in C_{1s} spectra at 284.7 eV (C–C, and C = C), 285.2 eV (C-O), and 288.7 eV (C = O).[45] Two peaks (Ag-$3d_{5/2}$ and Ag-$3d_{3/2}$) at 368.2 and 374.3 eV attributed to Ag-O and Ag-O-Ag confirmed the existence of Ag-BTC structure in both samples (Fig. 2e).[46] Two characteristic peaks around 954 and 932 eV for both Cu-MOF and GO-Cu-MOF represent the CuO ($2p_{1/2}$)[47] and Cu_2O ($2p_{3/2}$) (Fig. 2f).[48] In the GO-Cu-MOF sample, the epoxy group peak around 286.9 eV indicated the GO presence in the GO-Cu-MOF structure (Fig. 2c).[31] The presence of Cu ($2p_{3/2}$) and Cu ($2p_{1/2}$) at around 932 and 953 eV for both Cu-MOF and GO-Cu-MOF at high-resolution spectra confirms the formation of Cu-BTC.[49] Further investigation on the interaction between the rGO and MOF accomplished using the FT-IR spectrum as depicted in Fig. 2 g-j. The FTIR of rGO shows a broadband around 1600 cm^{-1} attributed to the phenyl C = C ring and sp^2 C = C bonds, which suggests the recovery of sp^2 lattice.[50] The peak for carboxyl groups in GO at 1700 cm^{-1} attributed to C = O stretching, the peak at 1066 cm^{-1} is attributed to C-O stretching, the peak at 1288 cm^{-1} is attributed to C-O-C bending, C-OH bending is at 1587 cm^{-1}, and a broad peak at 3448 cm^{-1} is attributed as O–H stretching vibration of the C-OH groups and water content in the material. The peaks at 1700, 1066, 1288 and 1587 suggest the presence of oxygen-containing functional groups in GO. The partially rGO spectra observations confirmed that most oxygen-containing functional groups in the GO were removed. The peak at 1066 disappears but peaks at 1288, 1724 and 3448, although present, have reduced intensities suggesting that some residual oxygen-functionalities on GO are still present on the partially rGO surface (Fig. 2g).[51] Two peaks at 1119 cm^{-1} and 954 cm^{-1} correspond to the BTC ring and the O–H in- and out-of-plane bending modes for Cu-MOF and GO-Cu-MOF, respectively [52] (Fig. 2h). Also, two additional peaks between 655 cm^{-1} and 731 cm^{-1} represent the BTC C–C ring out-of-plane mode. Three peaks at 1698, 1426, and 1390 cm^{-1} are related to the symmetric and asymmetric types of C = O of the carboxylic groups C-O and, respectively.[49,53] The peak shifts around 1390, 1426 and 1698 cm^{-1} can be justified because of the reaction between the BTC COOH group and copper ions during the formation of Cu-BTC. [52,54,55] The peak at 520 is related to the bending modes of Cu–O. In Fig. 2j, the peaks of C–H, and the C-O group are identified at 703–899 cm^{-1}, 1160 and 1192 cm^{-1}, respectively. The C = C stretching vibrations appeared in peaks around 1399–1474 cm^{-1}. The reaction

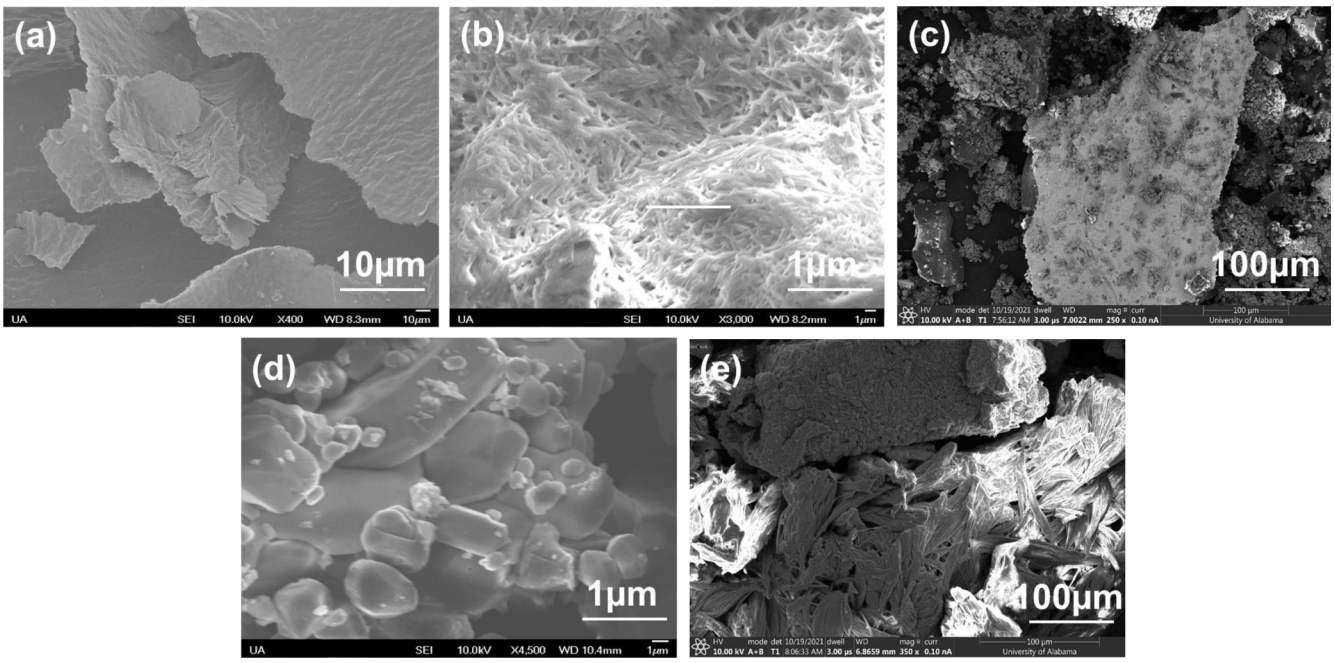

Fig. 3. SEM images of (a) GO, (b) Cu-MOF, (c) GO-Ag-MOF, (d) Ag-MOF, and (e) GO-Cu-MOF.

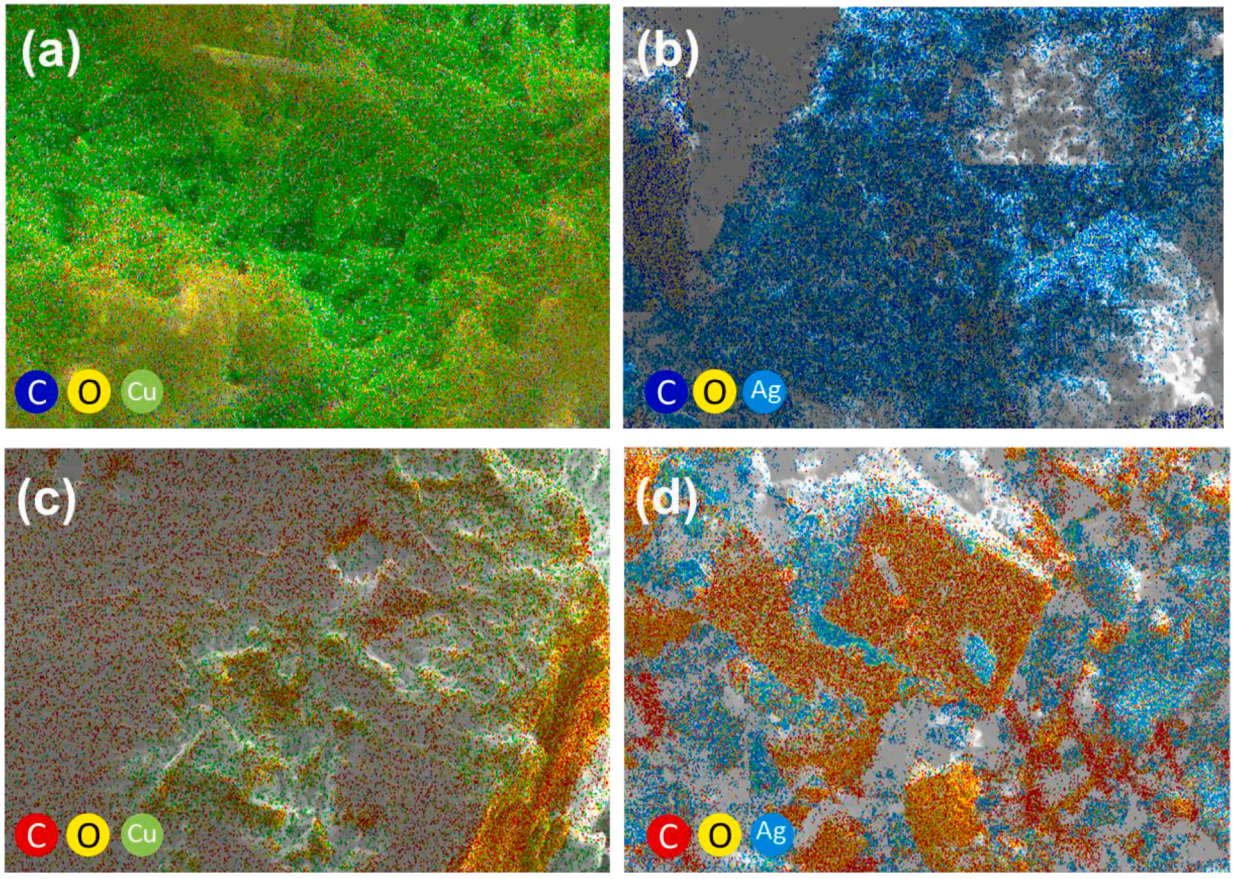

Fig. 4. EDX mapping of (a) Cu-MOF, (b) Ag-MOF, (c) GO-Cu-MOF, and (d) GO-Ag-MOF.

between carbonyl groups of BTC and silver ions were identified at peaks around 1678, and 1603 cm^{-1}.[31].

SEM images of GO and Cu-MOF revealed the typical morphology of plane sheet and needle-like, respectively, as reported in the literature [56,57], while Ag-MOF is observed to have cube-like crystals (Fig. 3). The SEM images of both GO-Ag-MOF and GO-Cu-MOF showed that Ag-MOF and Cu-MOF were synthesized on the GO sheet while they kept their normal cube-like and needle-like morphology. This is in agreement

Table 1
The BET plot test results of all the fabricated compounds.

Specimen	a_s, BET (m^2g^{-1})	A (cm^3g^{-1})	B (nm)
Cu-MOF	57	0.0704	7.62
GO-Cu-MOF	79	0.1051	7.75
Ag-MOF	86	0.0824	5.13
GO-Ag-MOF	114	0.1060	4.94

A = total pore volume
B = mean pore size

with XRD data of GO-Ag-MOF and GO-Cu-MOF showing the crystallinity of both Ag-MOF and Cu-MOF. The SEM images of GO-immobilized MOFs agree with the UV–Vis spectrum (Fig. 1 (b)), indicating Ag-MOF and Cu-MOF covered GO surface sheet. The uniform distribution of the copper and silver MOFs in the GO-Cu-MOF and GO-Ag-MOF was confirmed by EDX mapping showing no agglomeration occurred through the fabrication process (Fig. 4).

The porosity and surface area of the fabricated MOFs are presented in Table 1. The GO-Ag-MOF showed the highest surface area (a_s) (114 m^2g^{-1}) and Cu-MOF showed the lowest surface area (57 m^2g^{-1}) among the fabricated MOFs. The BET isotherms for all the MOFs follow a type IV isotherm trend which suggests the presence of mesopores in the material as shown in SI (Figure S3). The hysteresis loop of Cu-MOF and GO-Cu-MOF were broader compared to Ag-MOF and GO-Ag-MOF, suggesting the particle size distribution of Cu-based MOFs was broader and more dispersed, whereas both Ag-MOF and GO-Ag-MOF had no hysteresis loop, indicating the formation of uniform particles. The immobilization of both MOFs on the rGO resulted in enhanced surface area for both of them due to the addition of GO surface area to the compounds. The lower surface area of GO-Cu-MOF in comparison with GO-Ag-MOF was due to the lower surface area of Cu-MOF (57 m^2g^{-1}) compared to Ag-MOF (86 m^2g^{-1}). It was observed that by immobilization of MOF on rGO the pore size of Cu-MOF and Ag-MOF did not change, indicating the successful formation of MOFs on GO or inside GO without affecting the crystal structure of MOF. In addition, the surface area of GO (228 m^2g^{-1}) was reduced after immobilization of MOFs, which is another indication for successful synthesis of MOFs covering the surface of GO material.

Fig. 5 shows the Zeta potential of the fabricated MOFs (adsorbents) and MB dye (model adsorbate) at different pH values. Increasing the pH from 3 (acidic) to 10 (basic) resulted in increased negative zeta potential (surface charge) of MOFs due to the anionic nature of the adsorbents. The particles' surface charge increased in negative by immobilizing GO on both Ag-MOF and Cu-MOF, which can be attributed to the intrinsic negative surface charge of GO sheets[58]. GO-Ag-MOF showed the highest negative surface charge among the MOFs. Due to the cationic nature of MB, increasing the pH from 3 to 10 resulted in the reduction of MB positive Zeta potential over the pH range.

TGA analysis was performed to check the thermal stability of MOFs. Fig. 6 shows the TGA curves of Cu-MOF, GO-Cu-MOF, Ag-MOF and GO-Ag-MOF. Two major weight loss peaks were observed for the Cu-based MOFs similar to the literature [59,60]. The first weight loss around the temperature of 90–150 °C corresponds to the removal of moisture and other organic solvents, whereas the second weight loss peak around 300 °C is due to the degradation of organic linkers of BTC and decomposition to CuO [60]. The thermal stability of Cu-BTC was enhanced after the introduction of GO, with the decomposition temperature of GO-Cu-BTC increased to 350 from 300 °C. This temperature enhancement might be due to the presence of GO exfoliated sheets which improved the stability of the GO-Cu-MOF at higher temperatures [61]. For the Ag-based MOFs the slight weight loss around 150–200 °C could be due to the removal of solvent molecules encapsulated during the synthesis in MOF pores. The removal of these solvent molecules from MOFs at different temperatures can be attributed to the different porous structures of those MOFs [62]. The considerable weight loss around 350 °C could be attributed to the decomposition of BTC ligands from the framework and the formation of AgO. The introduction of GO increased the thermal and moisture stability of the GO-Cu-MOF compared to the Cu-MOF. The final degradation step at 350 °C for GO-Cu-MOF depicted a slower and less steep decomposition curve than Cu-MOF, which

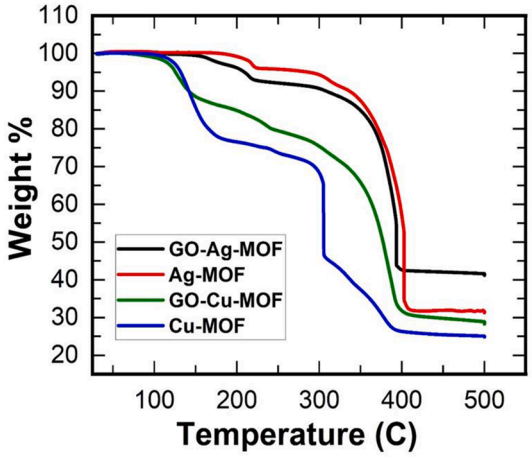

Fig. 6. Thermogravimetric analysis (TGA) of all MOFs from 30 to 500 °C with a heating rate of 10 °C min^{-1}.

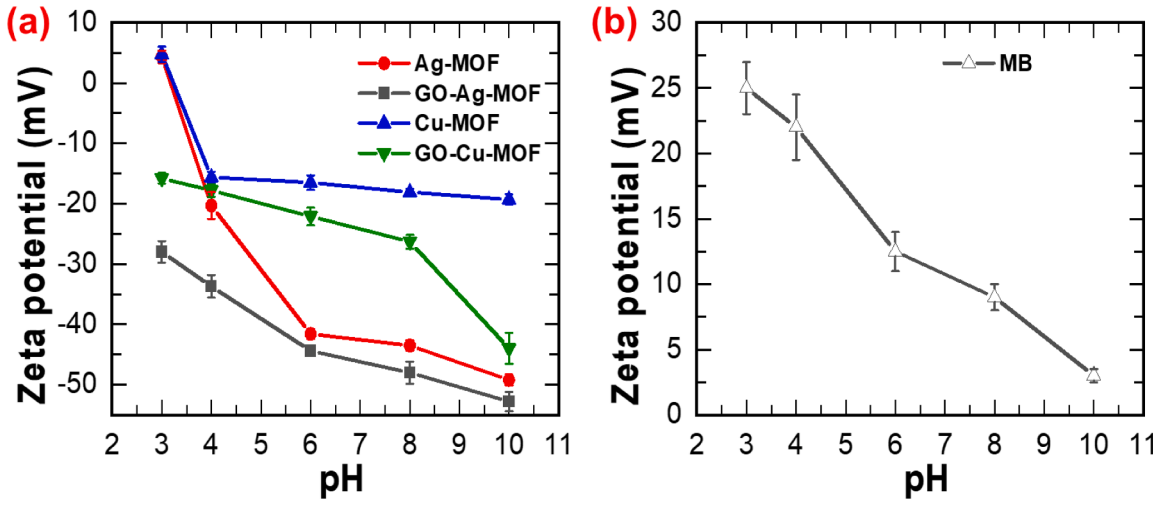

Fig. 5. Zeta Potential measurements of (a) all MOFs (adsorbents) and (b) MB solution at different pH values.

Table 2
The characteristic peaks of GO-Cu-MOF, Cu-MOF, GO-Ag-MOF, Ag-MOF, and dye loaded Ag-MOF, GO-Ag-MOF, GO-Cu-MOF, Cu-MOF NPs.

Specimen	$C=O$ Symmetric (cm^{-1})	$C=O$ Asymmetric (cm^{-1})	$C=C$(cm^{-1})	$C-O$ (cm^{-1})	$C-OH$ (cm^{-1})
Cu-MOF	1698	1426	1612	1390	1251
Cu-MOF-MB	1701	1428	1607	1385	1265
GO-Cu-MOF	1695	1425	1609	1387	1246
GO-Cu-MOF-MB	1706	1422	1615	1383	1265
Ag-MOF	–	1680	1474	–	–
Ag-MOF-MB	–	1678	1489	–	–
GO-Ag-MOF	–	1682	1471	–	–
GO-Ag-MOF-MB	–	1675	1489	–	–

indicates enhanced thermal stability of GO-Cu-MOF due to the strong interactions between GO and Cu-MOF[63]. GO/rGO was observed to be stable in the temperature range of 300–400 °C, which might be the reason for the increased thermal stability of the GO composite MOF.[64] In the case of GO-Ag-MOF the overall lower mass loss (55 %) compared to Ag-MOF (68 %) suggests that the strong interaction between GO and Ag-MOF has reduced the overall weight loss of the composite MOF thus reinforcing the MOF structure [61]. The DSC plots of all the MOFs (Figure S5) showed a distinct exothermic peak around 300 to 400 °C, which corresponds to the decomposition of the BTC ligands in the MOF. The exothermic peak shift from 300 °C in Cu-MOF to 400 °C in GO-Cu-MOF further signifies the improved thermal stability in the MOF. The endothermic peaks in all the MOFs correspond to the first weight loss step in TGA, indicating the dehydration process of the guest molecules [65].

3.2. Analytical Characterization of MOFs adsorption

Characterization techniques including FTIR and EdX mapping were used on the dye-loaded MOFs (adsorbate-adsorbent complex) after 24 hr of adsorption to confirm the presence of MB adsorbed onto the MOF. FTIR patterns on the dye-loaded materials confirmed similar peaks to that of MOFs before adsorption, but these peaks were slightly displaced due to the interaction of MB with the MOF. The FTIR spectra of loaded GO-Ag-MOF and GO-Cu-MOF illustrated the same trend. Characteristic peaks of all adsorbents are listed in Table 2. EDX map of dye-loaded GO-Cu-MOF and GO-Ag-MOF is displayed in Fig. 7. The sulfur map of the adsorbents showed the presence of sulfur in both samples. The amount of elemental sulfur detected by EDX mapping matched the number of sulfur atoms present in the molecular formula of MB, indicating the surface adsorption mechanism of MB on GO-MOF NPs.

3.3. Evaluation of MOFs adsorption mechanism and Kinetics

The adsorption capacity, mechanisms, and kinetics of fabricated MOFs towards MB, as the model of organic compounds in water treatment, were examined at different experimental conditions. Various isotherm adsorption experiments were conducted at different pH ranges from 3 to 10, different temperatures (25 °C and 45 °C), and different initial dye concentrations (10 ppm – 150 ppm).

3.3.1. Effect of pH on MOFs Adsorption

The adsorption of MB on all the adsorbents was observed to increase with increasing pH (Fig. 8). This trend was attributed to the electrostatic interaction between MB and the MOFs as one of the main surface adsorption mechanisms[66,67]. The electrostatic interaction between MOFs and MB can be justified based on the Zeta potential of MOFs and MB as described in Fig. 5. The zeta potential of all MOFs increased in negative value with an increase in pH, whereas MB had shown a reduction in positive zeta potential over all of the pH range. GO-Ag-MOF

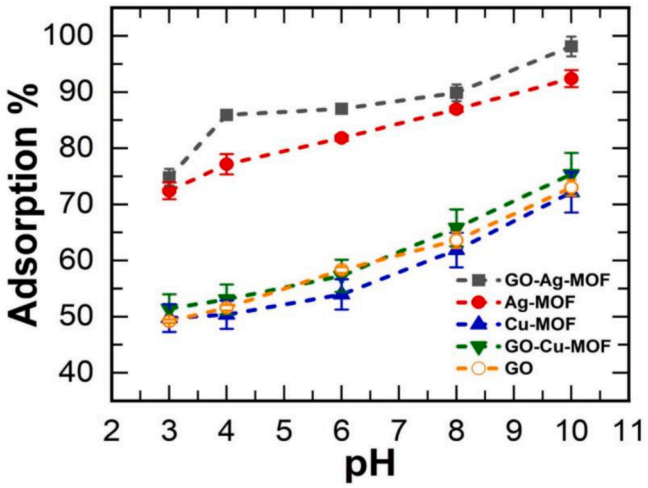

Fig. 8. Effect of pH on adsorption of MB on Cu-MOF, GO-Cu-MOF, Ag-MOF, and GO-Ag-MOF at the constant temperature of 25 °C. MB concentration of 70 mg/L and adsorbents concentration of 0.25 g/L.

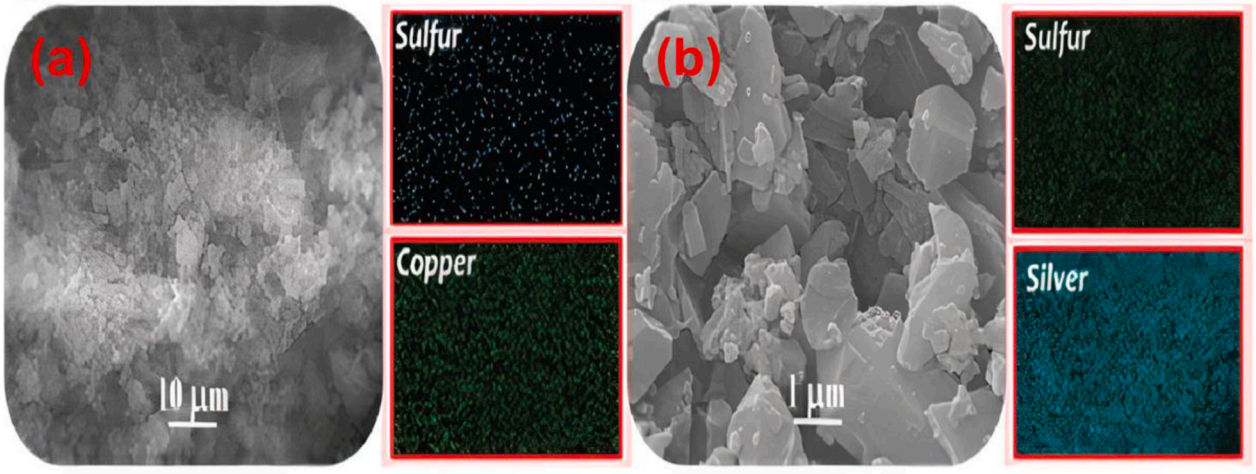

Fig. 7. EDX mapping of (a) GO-Cu-MOF, (b) GO-Ag-MOF after adsorption. The presence of sulfur on the EDX mapping of MOFs confirmed the adsorption of MB (adsorbate) on MOFs (adsorbents).

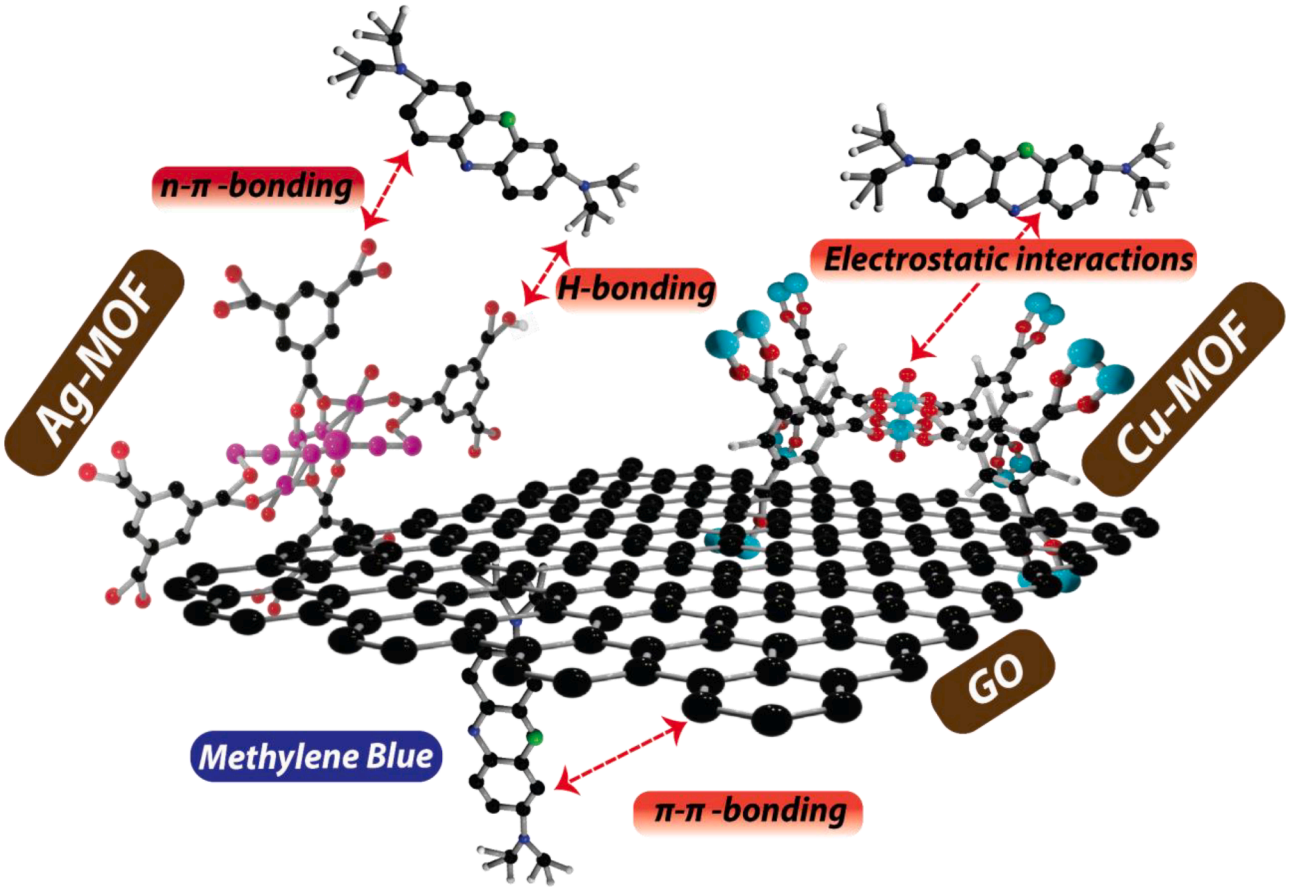

Fig. 9. Schematic showing effective interactions between GO-MOFs and MB during the adsorption process. Black represents carbon, red represents oxygen, white represents hydrogen, purple represents silver atoms, cyan represents copper atoms, blue represents nitrogen, and green represents the sulfur atoms. (For interpretation of the references to color in this figure legend, the reader is referred to the web version of this article.)

showed the highest adsorption capacity for the entire pH range compared to all the other adsorbents (Fig. 8). This result was in agreement with the measured Zeta potential of GO-Ag-MOF, as GO-Ag-MOF had the highest negative Zeta potential among all MOFs. The interaction between the methyl groups of MB and BTC carboxylate groups (for all samples) might be the reason for this behavior. [68] At pH = 5.6, when the pH of the solution is greater than the pH_{PZC}, both the carboxylic (pKa = 2–4) and phenolic groups (pKa = 8–9) undergo deprotonation and become negatively charged ligands, thus binding the positively charged MB indicating the presence of electrostatic interactions) and the presence of these extra-functional groups, such as the carbonyl groups of GO in GO-MOFs, increased the number of active adsorption sites for dye capturing, thus enhancing the GO-MOF adsorption capacities.[25] In addition, hydrogen bonding interactions can also occur between the MOFs and MB. Different types of hydrogen bonding, including the dipole–dipole hydrogen bonding, which forms between the surface hydrogens of hydroxyl groups and the nitrogen atoms of MB and Yoshida hydrogen bonding which occurs between the hydroxyl groups on MOFs and the aromatic rings of MB, are possible interactions for the adsorption (Fig. 9).[69] The dipole–dipole interactions can be confirmed by the slight decrease in intensity of peaks around 3400 cm^{-1} which represents the OH groups and the shift in the wavenumbers after MB adsorption as shown in SI (Figure S4) and Table 2.[69] Another possible interaction contributing to the adsorption of MB may be the π -π interaction between the benzene groups of MB and GO (Fig. 9)[70]. The n-π interactions of the carbonyl oxygens on the adsorbent surface with the aromatic rings of MB acting as electron donors and acceptors, respectively, can be the other interaction which is confirmed by the peak shifts to lower wavenumbers of C-O and C = O after adsorption in the FTIR as shown in Table 2. [50,70] Both GO-immobilized-MOFs showed a higher removal capacity in comparison to Cu-MOF and Ag- MOFs. This difference can also be attributed to the enhanced surface area of GO-immobilized MOF (Table 2). Another reason for lower adsorption of dye in acidic pH can be the deterioration of MOF and leaching of Cu and Ag from MOF structure at pH < 4 due to the lack of chemical stability of MOF.[71].

3.3.2. *Kinetics analysis of the MOFs isotherm adsorption*

Kinetic experiments were performed to determine the kinetics pattern of adsorption between MB and MOFs. More than 90% of adsorption was achieved in the first 4 h of contact time between MB and all four adsorbents, and an equilibrium state was achieved after 6 h for Ag-MOF and GO-Ag-MOF, whereas it took 12 h for Cu-MOF and GO-Cu-MOF to reach equilibrium. This different pattern might be due to the enhanced surface area and porous structure of Ag-MOF and GO-Ag-MOF compared to Cu-MOF or GO-Cu-MOF[71]. The uniform distribution of pores in Ag-MOF compared to Cu-MOF might have accelerated mass transfer, which resulted in a fast equilibrium for MB. Figure S6 displays the adsorption kinetics of MB on the synthesized MOFs. The transient concentration of MOFs versus time exhibits an almost similar trend for all the MOFs with higher adsorption capacity at the early stage of the adsorption process, due to the availability of a higher number of adsorption sites, and then approaches to equilibrium value almost in 6 hr. [72] As explained in Section 3.3.1, the enhanced adsorption capacity of both GO-immobilized MOFs in comparison to pure Cu-MOF and Ag-MOF may be attributed to the inclusion of GO in the fabrication of MOFs, which might lead to an increase in the hydrogen bonding and π-π interactions and more available active sites for MB to adsorb to GO. After

Table 3
Kinetic parameters of MB adsorption onto Ag-MOF, GO-Ag-MOF, GO-Cu-MOF and Cu-MOF.

Specimen	pseudo-first order $C_t = C_o - (C_o - C_e) \times (1 - e^{-k_1 t})$		pseudo-second order $C_t = C_o - (C_o - C_e) \times [1 - 1/(1 + k_2 t)]$	
	K_1 (min^{-1})	R^2	K_2 (min^{-1})	R^2
Cu-MOF	0.0992	0.7018	0.0037	0.9162
GO-Cu-MOF	0.0775	0.711	0.0031	0.9258
Ag-MOF	0.2395	0.8508	0.1743	0.9579
GO-Ag-MOF	0.2336	0.881	0.1846	0.9707

K_1 and K_2 are rate constants, C_o is the initial, C_t is transient, and C_e is the equilibrium concentrations of MB.

12 h, there was no considerable change in transient concentration which resulted in a lower share of physical adsorption.[73].

Pseudo-first-order, pseudo-second order, and intra-particle diffusion kinetic models were employed to explore the potential rate-controlling phenomenon in the adsorption of MB on MOFs. The equations of the pseudo-first order and pseudo-second-order kinetics models are expressed in Table 3. The parameters of pseudo-first-order kinetics model (K_1) and pseudo-second-order kinetics model (K_2) were determined from the linearized plots of C_t versus time as shown in Figure S7 and Fig. 10, respectively. GO-Ag-MOF and Ag-MOF possessed higher rate constants compared to the other MOFs correlating it to the larger surface area of the silver-based MOFs.[71] Curve fitting of experimental data resulted in a pseudo-second-order reaction which suggests the dominance of the chemisorption process. The chemisorption mechanism was supported by the zeta potential (Fig. 5), FTIR (Table 2) and EDX (Fig. 7) analysis as discussed earlier. (Table 3).[74].

Generally, the adsorption kinetics follows four consecutive steps. First, the adsorbate diffuses to the surface of the water film on the adsorbent surface from the bulk solution, and then the adsorbate overcomes the resistance of the liquid film on the adsorbent surface. The adsorbate then diffuses from the outer surface of the adsorbent to the adsorption site on the inner surface and finally reacts with the active site on the adsorbent. The intra-particle diffusion model proposed by Webber and Morris[75] quantifies the diffusion mechanism. The equation of the intra-particle diffusion model is expressed in Table 4. As shown in Table 4 q_t is the adsorption capacity in (mg/g), K_d is the intraparticle diffusion rate constant, and C is the intercept that correlates to the boundary layer thickness. In general, the intercept value (C) is

Table 4
Intra-particle diffusion model parameters of MB adsorption onto Ag-MOF, GO-Ag-MOF, GO-Cu-MOF and Cu-MOF.

Specimen	Intra-particle diffusion parameters $q_t = k_d t^{1/2} + C$					
	K_{d1} ($mg.g^{-1}min^{-0.5}$)	R^2	C_1	K_{d2} ($mg.g^{-1}min^{-0.5}$)	R^2	C_2
Cu-MOF	16.927	0.8332	2.703	2.4762	0.999	−74.14
GO-Cu-MOF	16.098	0.8581	2.22	2.2256	0.9963	−81.68
Ag-MOF	22.392	0.9197	1.49	0.9532	0.9988	−300.56
GO-Ag-MOF	20.664	0.979	1.06	0.8492	0.7152	−343.28

K_{d1} and K_{d2} are the intraparticle diffusion rate constants. q_t is the transient adsorption capacity of MB.

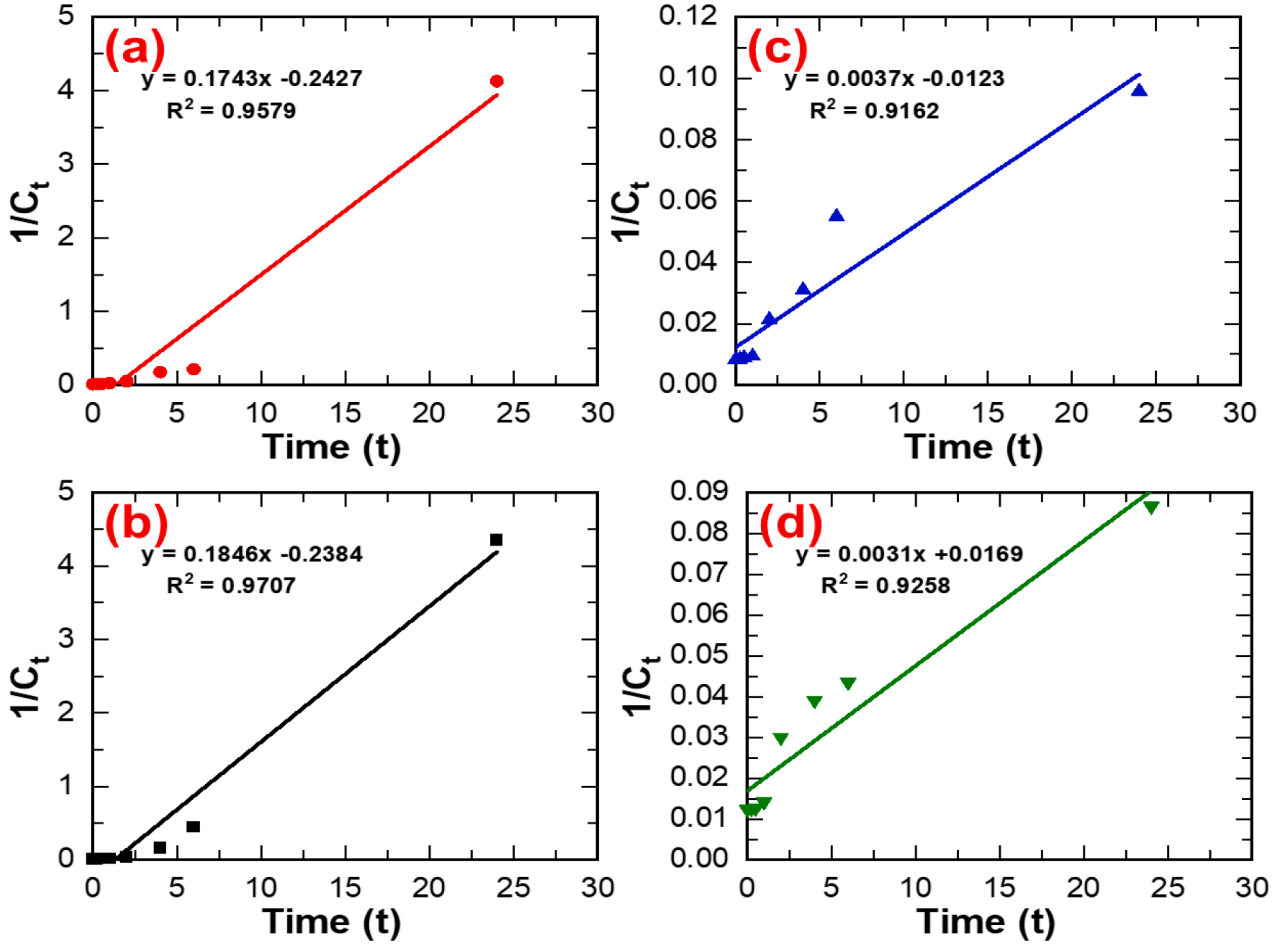

Fig. 10. Kinetic model fitting on (a) Ag-MOF, (b) GO-Ag-MOF, (c) Cu-MOF, and (d) GO-Cu-MOF at pH = 5.6. C_t is the transient concentration at time t.

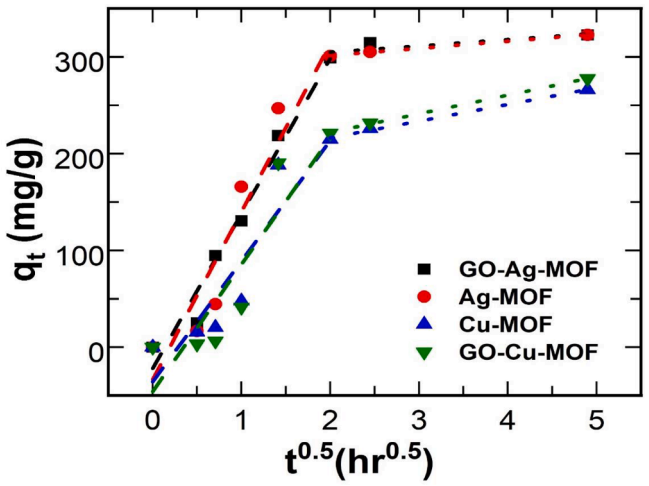

Fig. 11. Intra-particle diffusion model fitting for Ag-MOF, GO-Ag-MOF, Cu-MOF, and GO-Cu-MOF at pH = 5.6. C_t is the transient concentration at time t.

proportional to the extent of the boundary layer thickness effect on adsorbate transport. [76] The larger the intercept value (C) means, the more significant the boundary layer thickness effect (mass transport resistance).[77] Fig. 11 shows that the curve fit does not pass through the origin, suggesting more than one mechanism controlled the adsorption. The first region corresponds to external mass transfer and the second region corresponds to intraparticle diffusion.

The high K_{d1} values compared to K_{d2} values (Table 4) suggest that the rate of external mass transfer diffusion of MB onto the surface of MOF is faster than the rate of intraparticle diffusion and, therefore, the intraparticle diffusion is the rate-limiting step.[78] The intercept on time axis (C_1) shows the effect of boundary layer thickness on the external transport of MB towards MOFs. As shown in Table 4 the C_1 value is the lowest for GO-Ag-MOF (1.06) followed by Ag-MOF (1.49), GO-Cu-MOF (2.22) and Cu-MOF (2.703) suggesting that the mass transport resistance effects were more prominent in the Cu-based MOFs compared to Ag-based-MOFs thus confirming the superior adsorption capacity of Ag-based MOFs compared to Cu-based MOFs. The GO–incorporated materials were also observed to have a smaller boundary layer effect when compared to their counterparts without GO explaining their better adsorption capacity.

3.3.3. *Thermodynamics analysis of MOFs isotherms adsorption process*

Isotherm adsorption experiments were conducted at initial dye concentrations ranging from 10 ppm to 150 ppm and at two different temperatures of 25 °C and 45 °C to determine the effect of temperature and initial dye concentrations on the adsorption process. In general, the adsorption capacity of MOFs increased with increasing temperature suggesting that the adsorption of MB on MOFs is endothermic in nature that dissociates the water molecule from the surface of MOF.[67] As the initial dye concentration of MB solution increased, there was an increase in the adsorption capacity owing to a higher concentration gradient resulting in better mass transfer between adsorbents and MB (Fig. 12). [59] It was also observed that all the MOFs followed a similar trend, that GO-Ag-MOF had the highest adsorption capacity followed by Ag-MOF, GO-Cu-MOF, and Cu-MOF. The higher adsorption capacity of GO-Ag-MOF can be attributed to its higher adsorption surface area (Table 1)

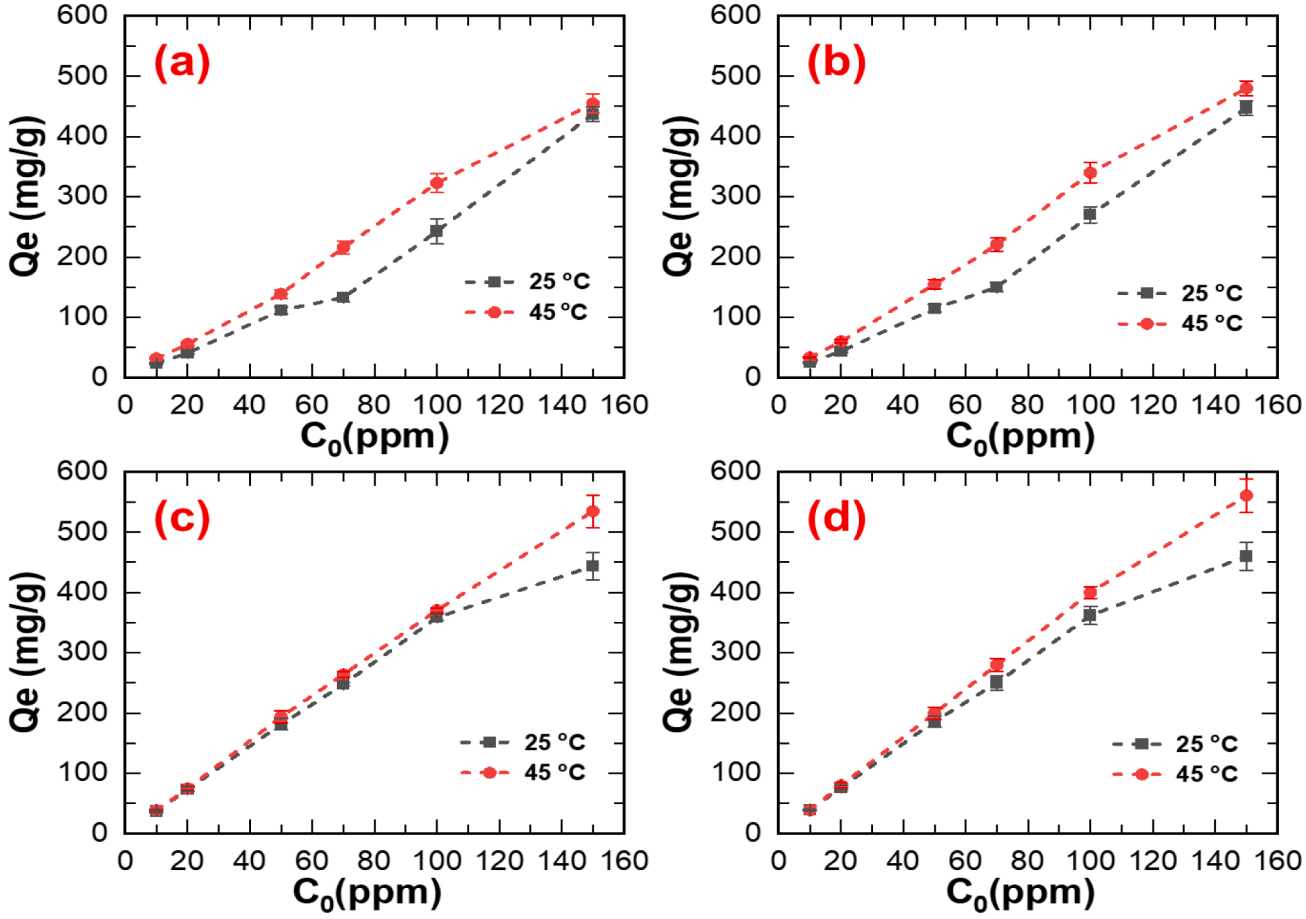

Fig. 12. Effect of MB initial concentration and temperature on (a) Cu-MOF (b) GO-Cu-MOF, (c) Ag-MOF, and (d) GO-Ag-MOF at pH = 5.6. Qe is dye concentration at equilibrium in the solid phase, C_0 is transient concentration, and Ce is equilibrium concentrations of MB.

Table 5
Thermodynamic parameters of MB adsorption onto Ag-MOF, GO-Ag-MOF, GO-Cu-MOF and Cu-MOF.

Specimen	ΔH_0 (KJmol^{-1})	ΔS_0 (JK^{-1}mol^{-1})	ΔG_0 (KJmol^{-1})	
			298 K	318 K
Cu-MOF	22.45	78.01	−0.81	−2.37
GO-Cu-MOF	19.4	69.23	−1.25	−2.63
Ag-MOF	4.57	27.2	−3.55	−4.09
GO-Ag-MOF	0.22	14.34	−4.06	−4.35

and higher surface negative charge (Fig. 5). This further confirms that the presence of GO increased the adsorption capacity of our MOFs under all conditions tested.

Thermodynamic parameters including ΔH_0, ΔS_0 and ΔG_0 were calculated for the MB adsorption process with all the MOFs as listed in Table 5. According to Table 5, ΔH_0 for all the MOFs shows a positive value indicating endothermic adsorptions. The adsorption process of MB with the MOFs can be confirmed to be a spontaneous process from the positive values of ΔS_0 and negative values of ΔG_0. ΔG_0 values decreased by increasing temperature, which suggests more efficient adsorption at a higher temperature. Also, the decrease of ΔG_0 by increasing temperature indicates more spontaneous reaction at higher temperature. The values of ΔH_0 and ΔS_0 for Ag-MOF and GO-Ag-MOF were higher compared with Cu-MOF and GO-Cu-MOF, which implies that more energy was required for the adsorption of Cu-based MOFs. This can also be confirmed with the inferior removal of MB using Cu-MOF and GO-Cu-MOF in comparison with Ag-MOF and GO-Ag-MOF (Fig. 8). The same trend was observed for GO-immobilized MOF that the ΔH_0 and ΔS_0 values of them were lower compared to Ag-MOF and Cu-MOF, implying that GO-MOFs had better adsorption capacities or dye removal capacities.[71].

The Temkin, Langmuir, and Freundlich models were fit to experimental isothermal data to examine the MOF adsorption behavior (Fig. 12 and Table 6). The maximum amount of adsorption (Q_{max}) following the Langmuir model for Cu-MOF, GO-Cu-MOF, Ag-MOF, and GO-Ag-MOF at 25 °C was 435, 476, 477, and 500 mg/g, respectively. All the MOFs adsorption behavior was fitted accurately in the Langmuir model, which presents the monolayer adsorption of adsorbates (MB) on MOFs. The Q_{max} for the Langmuir model for Cu-MOF, GO-Cu-MOF, Ag-MOF, and GO-Ag-MOF increased from 435 mg/g to 476 mg/g, 477 mg/g to 500 mg/g, 476 mg/g to 556 mg/g, and 500 mg/g to 625 mg/g, respectively by increasing the temperature from 25 °C to 45 °C. This trend in increased Q_{max} can be explained based on the fact that dye molecules penetration would be facilitated at higher temperatures due to the diffusion potential increment.[79].

3.4. Regeneration and Reusability

To evaluate the regenerability of MOF as an adsorbent, desorption (re-generability) experiments were performed using NaOH and water as eluents, and the effect of three consecutive adsorption–desorption cycles for a 12-hour time period was evaluated. There was around 10% decrease in adsorption efficiency after the first cycle for all the MOFs, but after the second cycle, no significant change in removal efficiency was observed. The GO-Ag-MOF showed the highest adsorption even after three cycles with a removal efficiency of more than 80% (Fig. 13), indicating that it was successfully regenerated for MB. The 10% portion of non-regenerated MOFs can be attributed to the chemisorption with strong chemical bonding between MB and MOF, which could not be regenerated. The removal efficiencies of regenerated MOFs followed the same trend as the fresh MOFs showed, with GO-Ag-MOF (85%) having the highest removal efficiency followed by Ag-MOF (73%), GO-Cu-MOF (54%), and Cu-MOF (49%) even after 3 cycles.

4. Conclusion

The Cu-MOF and Ag-MOF were synthesized using the fast and eco-friendly ultrasonic technique in the presence of GO resulting in immobilization of Cu-MOF and Ag-MOF on or inside the GO sheet and formation of GO-Cu-MOF and GO-Ag-MOF. The presence of GO in the in-

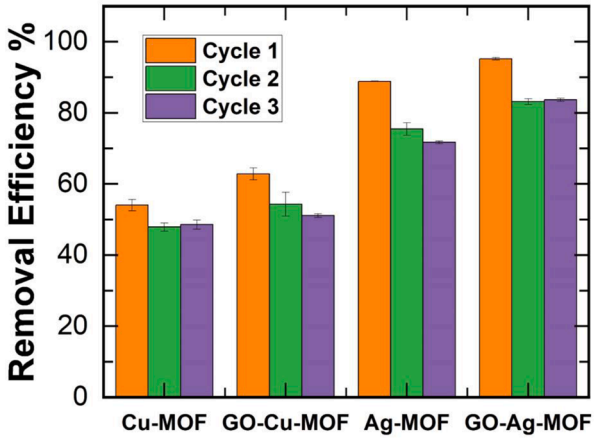

Fig. 13. Methylene Blue removal efficiency of the recycled MOFs. All MOFs were regenerated using NaOH for 12 h and a new cycle of adsorption was conducted for 12 h. Error bars represent the standard error of the mean. (For interpretation of the references to color in this figure legend, the reader is referred to the web version of this article.)

Table 6
Equilibrium parameters [a] for adsorption of MB onto Cu-MOF, GO-Cu-MOF, Ag-MOF, and GO-Ag-MOF.

T (°C)	Langmuir Equation $Q_e = \frac{Q_{max}K_LC_e}{1+K_LC_e}$			Freundlich Equation $Q_e = K_FC_e^{1/n}$			Temkin Equation $Q_e = BlnK_T + BlnC_e$		
	Q_{max} (mg/g)	K_L (L/mg)	R^2	K_F (mg$^{(1-1/n)}$L$^{1/n}$g^{-1})	N	R^2	B	K_T (L/mg)	R^2
Ag-MOF									
25	476	0.1212	0.99	58.15	1.55	0.94	106.87	1.62	0.94
45	556	0.1978	0.94	88.87	1.42	0.92	132.13	2.45	0.93
GO-Ag-MOF									
25	500	0.208	0.99	91.68	1.98	0.97	83.61	4.61	0.91
45	625	0.421	0.98	128.4	1.41	0.91	143.74	3.85	0.91
Cu-MOF									
25	435	0.014	0.97	4.15	0.91	0.86	122.85	0.2	0.54
45	476	0.034	0.94	13.68	1.04	0.94	131.26	0.38	0.77
GO-Cu-MOF									
25	477	0.017	0.93	5.79	0.94	0.90	128.72	0.23	0.60
45	500	0.042	0.94	17.23	1.04	0.95	144.11	0.46	0.78

situ synthesis of MOF did not affect the MOFs structure. The GO-Cu-MOF and GO-Ag-MOF showed enhanced physicochemical properties, including surface charge and surface area in comparison with pristine Cu-MOF and Ag-MOF. The practical application of all MOFs for water treatment as the adsorbents for dye removal was tested. In general, immobilization of Cu-MOF and Ag-MOF on GO sheets resulted in enhanced surface properties (surface charge, surface area, thermal stability, active adsorption sites) compared to their equivalent counterparts without GO. The GO-Ag-MOF showed the highest adsorption capacity among all adsorbents evaluated, exhibiting 98% dye removal. A study of the adsorption kinetics addressed the rapid adsorption process for all the adsorbents, generally < 4 hr. A multi-factor experimental study in which pH and temperature were varied showed that basic conditions (pH greater than 4) and high temperatures (45 ℃) were the optimum environments for the adsorption of MB to all MOF compounds. All MOFs showed only around 10% adsorption efficiency lost after three regeneration cycles.

Declaration of Competing Interest

The authors declare that they have no known competing financial interests or personal relationships that could have appeared to influence the work reported in this paper.

Acknowledgment

The authors would like to acknowledge the financial support of the United States Geological Survey (USGS) under Sponsor No. 20-WRC-207214 and to the Environmental Protection Agency (EPA) under Award No. 84014501. The authors gratefully thank the Department of Chemical and Biological Engineering at the University of Alabama and the Alabama Water Institute at the University of Alabama for research funding and instrumental support.

Appendix A. Supplementary data

Supplementary data to this article can be found online at https://doi.org/10.1016/j.cej.2022.135542.

References

[1] H. Li, M. Eddaoudi, M. O'Keeffe, O.M. Yaghi, Design and synthesis of an exceptionally stable and highly porous metal-organic framework, Nature 402 (6759) (1999) 276.
[2] A.H. Assen, O. Yassine, O. Shekhah, M. Eddaoudi, K.N. Salama, MOFs for the sensitive detection of ammonia: Deployment of fcu-MOF thin films as effective chemical capacitive sensors, ACS Sensors 2 (9) (2017) 1294–1301.
[3] A. Nasrollahpour, S. Moradi, Hexavalent chromium removal from water by ionic liquid modified metal-organic frameworks adsorbent, Microporous Mesoporous Mater. 243 (2017) 47–55.
[4] T. Le, X.i. Chen, H. Dong, W. Tarpeh, A. Perea-Cachero, J. Coronas, S.M. Martin, M. Mohammad, A. Razmjou, A.R. Esfahani, N. Koutahzadeh, P. Cheng, P. R. Kidambi, M.R. Esfahani, An Evolving Insight into Metal Organic Framework-Functionalized Membranes for Water and Wastewater Treatment and Resource Recovery, Ind. Eng. Chem. Res. 60 (19) (2021) 6869–6907.
[5] S. Achmann, G. Hagen, M. Haemmerle, I. Malkowsky, C. Kiener, R. Moos, Sulfur Removal from Low-Sulfur Gasoline and Diesel Fuel by Metal-Organic Frameworks, Chemical Engineering & Technology: Industrial Chemistry-Plant Equipment-Process Engineering-Biotechnology 33 (2) (2010) 275–280.
[6] M. Maes, F. Vermoortele, L. Alaerts, J.F. Denayer, D.E. De Vos, Separating saturated alkylaromatics from their unsaturated analogues using metal– organic frameworks, The Journal of Physical Chemistry C 115 (4) (2010) 1051–1055.
[7] Z.J. Parkerson, T. Le, P. Das, S.N. Mahmoodi, M.R. Esfahani, Cu-MOF-Polydopamine-Incorporated Functionalized Nanofiltration Membranes for Water Treatment: Effect of Surficial Adhesive Modification Techniques, ACS ES&T Water 1 (2) (2020) 430–439.
[8] J. Jiang, R. Babarao, Z. Hu, Molecular simulations for energy, environmental and pharmaceutical applications of nanoporous materials: from zeolites, metal–organic frameworks to protein crystals, Chem. Soc. Rev. 40 (7) (2011) 3599–3612.
[9] N.A. Khan, Z. Hasan, S.H. Jhung, Adsorptive removal of hazardous materials using metal-organic frameworks (MOFs): a review, J. Hazard. Mater. 244 (2013) 444–456.
[10] A. Jeyaseelan, M.u. Naushad, T. Ahamad, N. Viswanathan, Design and development of amine functionalized iron based metal organic frameworks for selective fluoride removal from water environment, J. Environ. Chem. Eng. 9 (1) (2021) 104563.
[11] A. Jeyaseelan, N. Viswanathan, Design of amino-functionalized benzene-1, 4-dicarboxylic acid-fabricated lanthanum-based metal–organic frameworks for defluoridation of water, J. Chem. Eng. Data 65 (11) (2020) 5328–5340.
[12] A. Jeyaseelan, N. Viswanathan, Facile synthesis of tunable rare earth based metal organic frameworks for enhanced fluoride retention, J. Mol. Liq. 326 (2021), 115163.
[13] K. Iman, M. Shahid, M.S. Khan, M. Ahmad, F. Sama, Topology, magnetism and dye adsorption properties of metal organic frameworks (MOFs) synthesized from bench chemicals, CrystEngComm 21 (35) (2019) 5299–5309, https://doi.org/10.1039/C9CE01041F.
[14] M. Shahnawaz Khan, M. Khalid, M. Shahid, What triggers dye adsorption by metal organic frameworks? The current perspectives, Mater. Adv. 1 (6) (2020) 1575–1601.
[15] E.M. Dias C. Petit Correction: Towards the use of metal–organic frameworks for water reuse: a review of the recent advances in the field of organic pollutants removal and degradation and the next steps in the field Journal of Materials Chemistry A 4 9 2016 3565 3565.
[16] M.D. Firouzjaei, F.A. Afkhami, M.R. Esfahani, C.H. Turner, S. Nejati, Experimental and molecular dynamics study on dye removal from water by a graphene oxide-copper-metal organic framework nanocomposite, J. Water Process Eng. 34 (2020), 101180.
[17] M.R. Esfahani, S.A. Aktij, Z. Dabaghian, M.D. Firouzjaei, A. Rahimpour, J. Eke, I. C. Escobar, M. Abolhassani, L.F. Greenlee, A.R. Esfahani, A. Sadmani, N. Koutahzadeh, Nanocomposite membranes for water separation and purification: Fabrication, modification, and applications, Sep. Purif. Technol. 213 (2019) 465–499.
[18] D. Wang, J. Zhang, G. Li, J. Yuan, J. Li, Q. Huo, Y. Liu, Mesoporous Hexanuclear Copper Cluster-Based Metal-Organic Framework with Highly Selective Adsorption of Gas and Organic Dye Molecules, ACS Appl. Mater. Interfaces 10 (37) (2018) 31233–31239.
[19] C. Li, Z. Xiong, J. Zhang, C. Wu, The strengthening role of the amino group in metal–organic framework MIL-53 (Al) for methylene blue and malachite green dye adsorption, J. Chem. Eng. Data 60 (11) (2015) 3414–3422.
[20] S. Franzen, J.C.W. Folmer, W.R. Glomm, R. O'Neal, Optical Properties of Dye Molecules Adsorbed on Single Gold and Silver Nanoparticles, The Journal of Physical Chemistry A 106 (28) (2002) 6533–6540, https://doi.org/10.1021/jp025536g.
[21] M.K. Satapathy, P. Banerjee, P. Das, Plant-mediated synthesis of silver-nanocomposite as novel effective azo dye adsorbent, Applied Nanoscience 5 (1) (2015) 1–9.
[22] L. Azeez, A. Lateef, S.A. Adebisi, A.O. Oyedeji, Novel biosynthesized silver nanoparticles from cobweb as adsorbent for Rhodamine B: equilibrium isotherm, kinetic and thermodynamic studies, Appl. Water Sci. 8 (1) (2018) 1–12.
[23] M. Ghaedi, B. Sadeghian, A.A. Pebdani, R. Sahraei, A. Daneshfar, C. Duran, Kinetics, thermodynamics and equilibrium evaluation of direct yellow 12 removal by adsorption onto silver nanoparticles loaded activated carbon, Chem. Eng. J. 187 (2012) 133–141.
[24] A. AbdEl-Salam, H. Ewais, A. Basaleh, Silver nanoparticles immobilised on the activated carbon as efficient adsorbent for removal of crystal violet dye from aqueous solutions, A kinetic study, Journal of Molecular Liquids 248 (2017) 833–841.
[25] I. Mantasha, H.A. Saleh, K.M. Qasem, M. Shahid, M. Mehtab, M. Ahmad, Efficient and selective adsorption and separation of methylene blue (MB) from mixture of dyes in aqueous environment employing a Cu (II) based metal organic framework, Inorg. Chim. Acta 511 (2020), 119787.
[26] A.R. Abbasi, M. Karimi, K. Daasbjerg, Efficient removal of crystal violet and methylene blue from wastewater by ultrasound nanoparticles Cu-MOF in comparison with mechanosynthesis method, Ultrason. Sonochem. 37 (2017) 182–191.
[27] J. Duan, S. Chen, M. Jaroniec, S.Z. Qiao, Heteroatom-doped graphene-based materials for energy-relevant electrocatalytic processes, ACS Catal. 5 (9) (2015) 5207–5234.
[28] A. Abd-Elhamid, E.A. Kamoun, A.A. El-Shanshory, H.M. Soliman, H. Aly, Evaluation of graphene oxide-activated carbon as effective composite adsorbent toward the removal of cationic dyes: Composite preparation, characterization and adsorption parameters, J. Mol. Liq. 279 (2019) 530–539.
[29] W. Konicki, M. Aleksandrzak, D. Moszyński, E. Mijowska, Adsorption of anionic azo-dyes from aqueous solutions onto graphene oxide: equilibrium, kinetic and thermodynamic studies, J. Colloid Interface Sci. 496 (2017) 188–200.
[30] R. Guo, T. Jiao, R. Li, Y. Chen, W. Guo, L. Zhang, J. Zhou, Q. Zhang, Q. Peng, Sandwiched Fe3O4/carboxylate graphene oxide nanostructures constructed by layer-by-layer assembly for highly efficient and magnetically recyclable dye removal, ACS Sustainable Chem. Eng. 6 (1) (2017) 1279–1288.
[31] M.D. Firouzjaei, A.A. Shamsabadi, M. Sharifian Gh, A. Rahimpour, M. Soroush, A novel nanocomposite with superior antibacterial activity: a silver-based metal organic framework embellished with graphene oxide, Advanced Materials, Interfaces 5 (11) (2018) 1701365.
[32] G.Z. Kyzas, K.A. Matis, Nanoadsorbents for pollutants removal: a review, J. Mol. Liq. 203 (2015) 159–168.
[33] A.M. Aljeboree, A.N. Alshirifi, A.F. Alkaim, Kinetics and equilibrium study for the adsorption of textile dyes on coconut shell activated carbon, Arabian J. Chem. 10 (2017) S3381–S3393.

[34] T. Maneerung, J. Liew, Y. Dai, S. Kawi, C. Chong, C.-H. Wang, Activated carbon derived from carbon residue from biomass gasification and its application for dye adsorption: kinetics, isotherms and thermodynamic studies, Bioresour. Technol. 200 (2016) 350–359.
[35] S. Marx, W. Kleist, A. Baiker, Synthesis, structural properties, and catalytic behavior of Cu-BTC and mixed-linker Cu-BTC-PyDC in the oxidation of benzene derivatives, J. Catal. 281 (1) (2011) 76–87.
[36] N. Iqbal, X. Wang, J. Yu, N. Jabeen, H. Ullah, B. Ding, In situ synthesis of carbon nanotube doped metal–organic frameworks for CO 2 capture, RSC Adv. 6 (6) (2016) 4382–4386.
[37] V. Jabbari, J. Veleta, M. Zarei-Chaleshtori, J. Gardea-Torresdey, D. Villagrán, Green synthesis of magnetic MOF@ GO and MOF@ CNT hybrid nanocomposites with high adsorption capacity towards organic pollutants, Chem. Eng. J. 304 (2016) 774–783.
[38] A.A. Jeffery, S.R. Rao, M. Rajamathi, Preparation of MoS2–reduced graphene oxide (rGO) hybrid paper for catalytic applications by simple exfoliation–costacking, Carbon 112 (2017) 8–16.
[39] H. Guo, Y. Zhang, Z. Zheng, H. Lin, Y. Zhang, Facile one-pot fabrication of Ag@ MOF (Ag) nanocomposites for highly selective detection of 2, 4, 6-trinitrophenol in aqueous phase, Talanta 170 (2017) 146–151.
[40] S. Gurunathan, J.W. Han, A.A. Dayem, V. Eppakayala, J.-H. Kim, Oxidative stress-mediated antibacterial activity of graphene oxide and reduced graphene oxide in Pseudomonas aeruginosa, Int. J. Nanomed. 7 (2012) 5901.
[41] X. Wang, Q. Wang, Q. Wang, F. Gao, F. Gao, Y. Yang, H. Guo, Highly dispersible and stable copper terephthalate metal–organic framework–graphene oxide nanocomposite for an electrochemical sensing application, ACS Appl. Mater. Interfaces 6 (14) (2014) 11573–11580.
[42] P. Karthik, R. Vinoth, P. Zhang, W. Choi, E. Balaraman, B. Neppolian, π–π Interaction Between Metal-Organic Framework and Reduced Graphene Oxide for Visible-Light Photocatalytic H2 Production, ACS Applied Energy Materials 1 (5) (2018) 1913–1923.
[43] R. Thakuria, N.K. Nath, B.K. Saha, The Nature and Applications of π–π Interactions: A Perspective, Cryst. Growth Des. 19 (2) (2019) 523–528.
[44] G. Mahalakshmi, V. Balachandran, FT-IR and FT-Raman spectra, normal coordinate analysis and ab initio computations of Trimesic acid, Spectrochim. Acta Part A Mol. Biomol. Spectrosc. 124 (2014) 535–547.
[45] S. Pei, H.-M. Cheng, The reduction of graphene oxide, Carbon 50 (9) (2012) 3210–3228.
[46] A.M. Ferraria, A.P. Carapeto, A.M.B. do Rego,, X-ray photoelectron spectroscopy: silver salts revisited, Vacuum 86 (12) (2012) 1988–1991.
[47] J.G. Jolley, G.G. Geesey, M.R. Hankins, R.B. Wright, P.L. Wichlacz, Auger electron and X-ray photoelectron spectroscopic study of the biocorrosion of copper by alginic acid polysaccharide, Appl. Surf. Sci. 37 (4) (1989) 469–480.
[48] D. Chadwick, T. Hashemi, Adsorbed corrosion inhibitors studied by electron spectroscopy: benzotriazole on copper and copper alloys, Corros. Sci. 18 (1) (1978) 39–51.
[49] J. Cheng, X. Xuan, X. Yang, J. Zhou, K. Cen, Preparation of a Cu (BTC)-rGO catalyst loaded on a Pt deposited Cu foam cathode to reduce CO 2 in a photoelectrochemical cell, RSC Adv. 8 (56) (2018) 32296–32303.
[50] S. Liu, L.-X. Sun, L.-T. Liu, Y.-L. Zhou, F. Xu, Morphology-control synthesis of a Cu-based metal–organic framework directed by carboxyl-functionalized graphene, Polyhedron 149 (2018) 104–108.
[51] E. Andrijanto, S. Shoelarta, G. Subiyanto, S. Rifki, Facile synthesis of graphene from graphite using ascorbic acid as reducing agent, AIP Conference Proceedings, AIP Publishing LLC (2016), 020003.
[52] R.M. Abdelhameed, H.E. Emam, J. Rocha, A.M. Silva, Cu-BTC metal-organic framework natural fabric composites for fuel purification, Fuel Process. Technol. 159 (2017) 306–312.
[53] D. Zhao, P. Wang, Q. Zhao, N. Chen, X. Lu, Thermoresponsive copolymer-based draw solution for seawater desalination in a combined process of forward osmosis and membrane distillation, Desalination 348 (2014) 26–32.
[54] J.B. DeCoste, G.W. Peterson, B.J. Schindler, K.L. Killops, M.A. Browe, J.J. Mahle, The effect of water adsorption on the structure of the carboxylate containing metal–organic frameworks Cu-BTC, Mg-MOF-74, and UiO-66, J. Mater. Chem. A 1 (38) (2013) 11922–11932.
[55] H. Noei, S. Amirjalayer, M. Müller, X. Zhang, R. Schmid, M. Muhler, R.A. Fischer, Y. Wang, Low-Temperature CO Oxidation over Cu-Based Metal-Organic Frameworks Monitored by using FTIR Spectroscopy, ChemCatChem 4 (6) (2012) 755–759.
[56] A. Akbari, J. Karimi-Sabet, S.M. Ghoreishi, Intensification of helium separation from CH4 and N2 by size-reduced Cu-BTC particles in Matrimid matrix, Sep. Purif. Technol. 251 (2020) 117317.
[57] C. Manoratne, S. Rosa, I. Kottegoda, XRD-HTA, UV visible, FTIR and SEM interpretation of reduced graphene oxide synthesized from high purity vein graphite, Material Science Research India 14(1) (2017) 19-30.
[58] D.R. Dreyer, S. Park, C.W. Bielawski, R.S. Ruoff, The chemistry of graphene oxide, Chem. Soc. Rev. 39 (1) (2010) 228–240.
[59] R. Kaur, A. Kaur, A. Umar, W.A. Anderson, S.K. Kansal, Metal organic framework (MOF) porous octahedral nanocrystals of Cu-BTC: synthesis, properties and enhanced adsorption properties, Mater. Res. Bull. 109 (2019) 124–133.
[60] S. Khoshhal, A.A. Ghoreyshi, M. Jahanshahi, M. Mohammadi, Study of the temperature and solvent content effects on the structure of Cu–BTC metal organic framework for hydrogen storage, RSC Adv. 5 (31) (2015) 24758–24768.
[61] Z. Liu, Z. Chen, F. Yu, Enhanced thermal conductivity of microencapsulated phase change materials based on graphene oxide and carbon nanotube hybrid filler, Sol. Energy Mater. Sol. Cells 192 (2019) 72–80.
[62] H.A. Ozen, B. Ozturk, Gas separation characteristic of mixed matrix membrane prepared by MOF-5 including different metals, Sep. Purif. Technol. 211 (2019) 514–521.
[63] M.D. Makhafola, K.E. Ramohlola, T.C. Maponya, T.R. Somo, E.I. Iwuoha, K. Makgopa, M.J. Hato, K.M. Molapo, K.D. Modibane, Electrocatalytic activity of graphene oxide/metal organic framework hybrid composite on hydrogen evolution reaction properties, Int. J. Electrochem. Sci 15 (2020) 4884–4899.
[64] S.N. Alam, N. Sharma, L. Kumar, Synthesis of graphene oxide (GO) by modified hummers method and its thermal reduction to obtain reduced graphene oxide (rGO), Graphene 6 (1) (2017) 1–18.
[65] L. Gong, G. Chen, Y. Liu, T. Wang, J. Zhang, X. Yi, P. He, Energetic metal–organic frameworks achieved from furazan and triazole ligands: synthesis, crystal structure, thermal stability and energetic performance, New J. Chem. 45 (47) (2021) 22299–22305.
[66] W. Zhang, R.-Z. Zhang, Y.-Q. Huang, J.-M. Yang, Effect of the synergetic interplay between the electrostatic interactions, size of the dye molecules, and adsorption sites of MIL-101 (Cr) on the adsorption of organic dyes from aqueous solutions, Cryst. Growth Des. 18 (12) (2018) 7533–7540.
[67] H. Molavi, A. Hakimian, A. Shojaei, M. Raeiszadeh, Selective dye adsorption by highly water stable metal-organic framework: Long term stability analysis in aqueous media, Appl. Surf. Sci. 445 (2018) 424–436.
[68] J. Singh, G. Kaur, M. Rawat, A brief review on synthesis and characterization of copper oxide nanoparticles and its applications, J. Bioelectron. Nanotechnol 1 (9) (2016).
[69] H.N. Tran, S.-J. You, H.-P. Chao, Insight into adsorption mechanism of cationic dye onto agricultural residues-derived hydrochars: negligible role of π-π interaction, Korean J. Chem. Eng. 34 (6) (2017) 1708–1720.
[70] V.-P. Dinh, H.M. Le, V.-D. Nguyen, V.-A. Dao, N.Q. Hung, L.A. Tuyen, S. Lee, J. Yi, T.D. Nguyen, L. Tan, Insight into the adsorption mechanisms of methylene blue and chromium (III) from aqueous solution onto pomelo fruit peel, RSC Adv. 9 (44) (2019) 25847–25860.
[71] B.-L. Zhang, W. Qiu, P.-P. Wang, Y.-L. Liu, J. Zou, L. Wang, J. Ma, Mechanism study about the adsorption of Pb (II) and Cd (II) with iron-trimesic metal-organic frameworks, Chem. Eng. J. 385 (2020), 123507.
[72] E. Haque, J.E. Lee, I.T. Jang, Y.K. Hwang, J.-S. Chang, J. Jegal, S.H. Jhung, Adsorptive removal of methyl orange from aqueous solution with metal-organic frameworks, porous chromium-benzenedicarboxylates, J. Hazard. Mater. 181 (1–3) (2010) 535–542.
[73] T.W. Seow, C.K. Lim, Removal of dye by adsorption: a review, International Journal of Applied Engineering Research 11 (4) (2016) 2675–2679.
[74] C. Arora, S. Soni, S. Sahu, J. Mittal, P. Kumar, P. Bajpai, Iron based metal organic framework for efficient removal of methylene blue dye from industrial waste, J. Mol. Liq. 284 (2019) 343–352.
[75] W.J. Weber Jr, J.C. Morris, Kinetics of adsorption on carbon from solution, Journal of the sanitary engineering division 89 (2) (1963) 31–59.
[76] G. Mckay, M. Otterburn, A. Sweeney, The removal of colour from effluent using various adsorbents—III. Silica: Rate processes, Water Res. 14 (1) (1980) 15–20.
[77] G. Mckay, The adsorption of dyestuffs from aqueous solutions using activated carbon. III. Intraparticle diffusion processes, Journal of Chemical Technology and Biotechnology, Chemical Technology 33 (4) (1983) 196–204.
[78] L.R. Arenas, S.R. Gentile, S. Zimmermann, S. Stoll, Nanoplastics adsorption and removal efficiency by granular activated carbon used in drinking water treatment process, Sci. Total Environ. 791 (2021), 148175.
[79] Z. Cheng, J. Liao, B. He, F. Zhang, F. Zhang, X. Huang, L. Zhou, One-step fabrication of graphene oxide enhanced magnetic composite gel for highly efficient dye adsorption and catalysis, ACS Sustainable Chem. Eng. 3 (7) (2015) 1677–1685.

Supplementary Information

Silver Metal Organic Frameworks and Copper Metal Organic Frameworks Immobilized on Graphene oxide for Enhanced Adsorption in Water Treatment

Medha Kasula [a], Tin Le [a], Adrienne Thomsen [a], Milad Rabbani Esfahani [*a]

[a] Department of Chemical and Biological Engineering, University of Alabama, Tuscaloosa, United States

*Corresponding Author:
Milad Rabbani Esfahani
mesfahani@eng.ua.edu
Phone# 205-348-8836

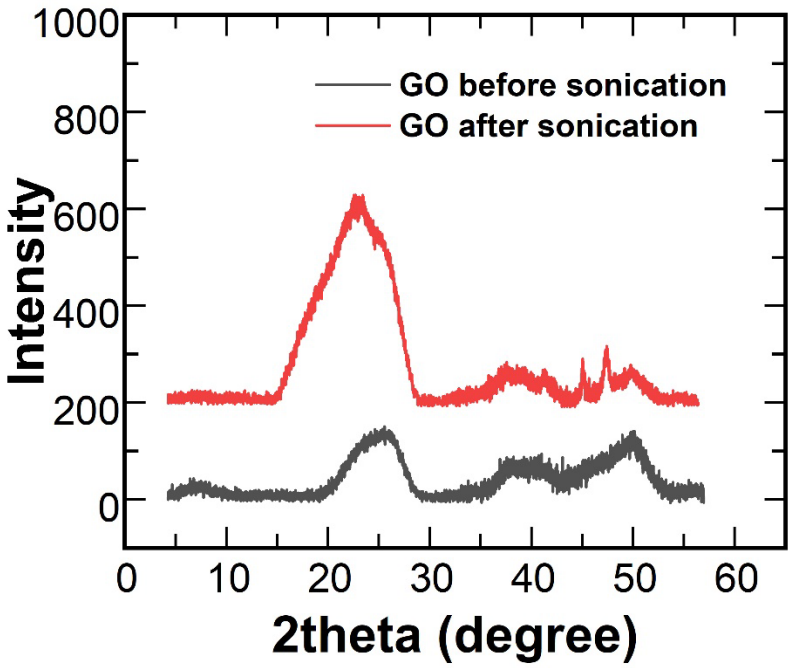

Figure S1. XRD of GO before sonication and after sonication

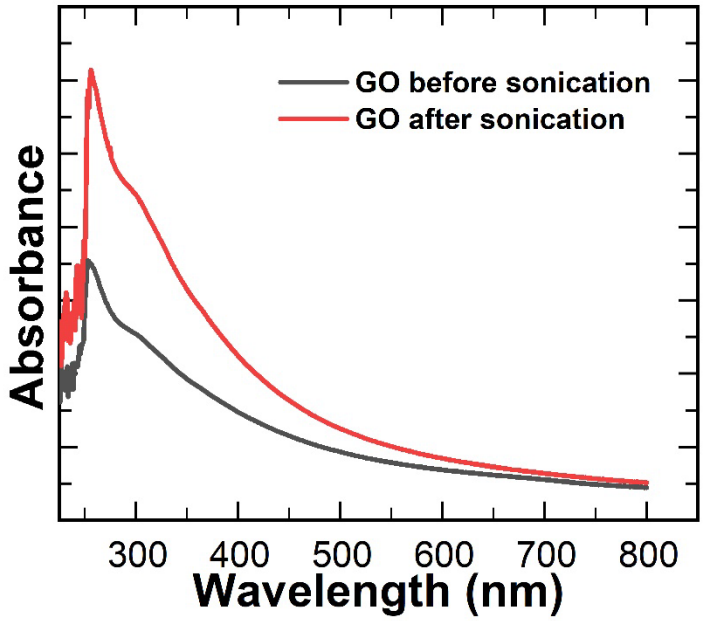

Figure S2. UV-Vis of GO before sonication and after sonication

The atomic concentrations of the GO-Cu-MOF, GO, Cu-MOF, Ag-MOF, and GO-Ag-MOF were tabulated in **Table S1**.

Table S1. The Elemental Composition of GO-Cu-MOF, Cu-MOF, Ag-MOF, and GO-Ag-MOF extracted from high-resolution XPS spectra.

Specimen	*Carbon*		*Oxygen*		*Copper*		*Silver*	
	Wt.%	*Atomic%*	*Wt.%*	*Atomic%*	*Wt.%*	*Atomic%*	*Wt.%*	*Atomic%*
GO	*61.53*	*68.08*	*38.47*	*31.94*	-	-	-	-
Cu-MOF	*71.65*	*60.38*	*26.01*	*29.2*	*2.34*	*10.34*	-	-
GO-Cu-MOF	*63.05*	*72.30*	*26.30*	*30.55*	*1.4*	*6.4*	-	-
Ag-MOF	*69.1*	*58.83*	*28.29*	*31.23*	-	-	*2.61*	*8.95*
GO-Ag-MOF	*57.4*	*63.51*	*40.63*	*31.06*	-	-	*1.97*	*5.43*

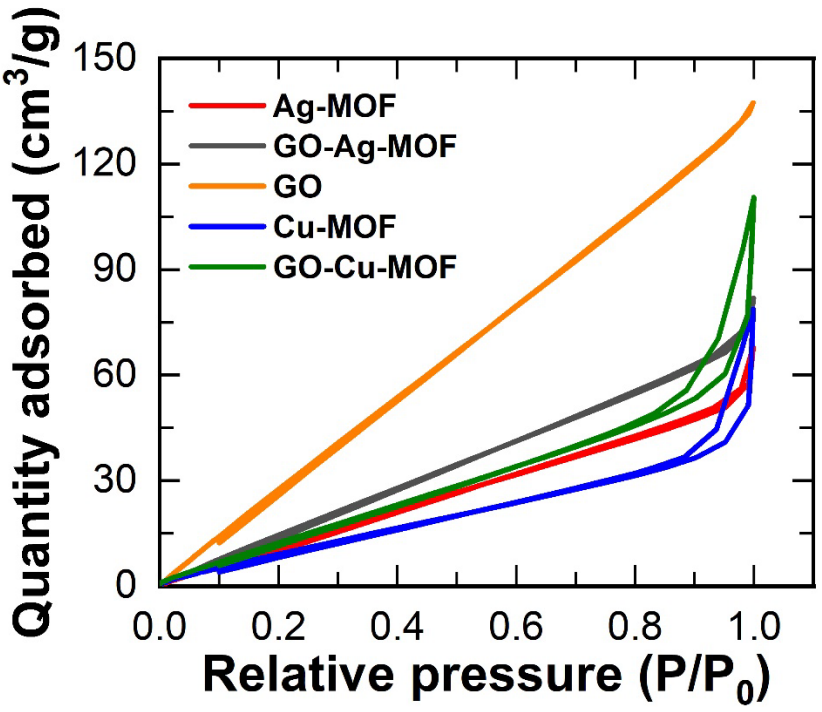

Figure S3. BET isotherms of GO, Ag-MOF, GO-Ag-MOF, Cu-MOF and GO-Cu-MOF

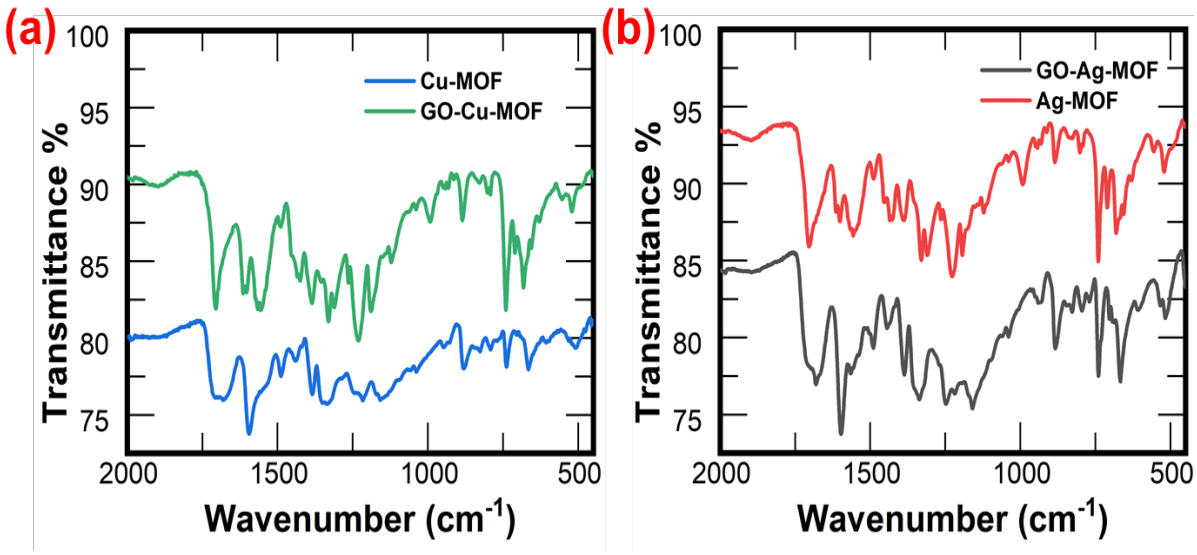

Figure S4. FTIR spectra of loaded dye samples (a) Cu-MOF, GO-Cu-MOF and (b) Ag-MOF, GO-Ag-MOF

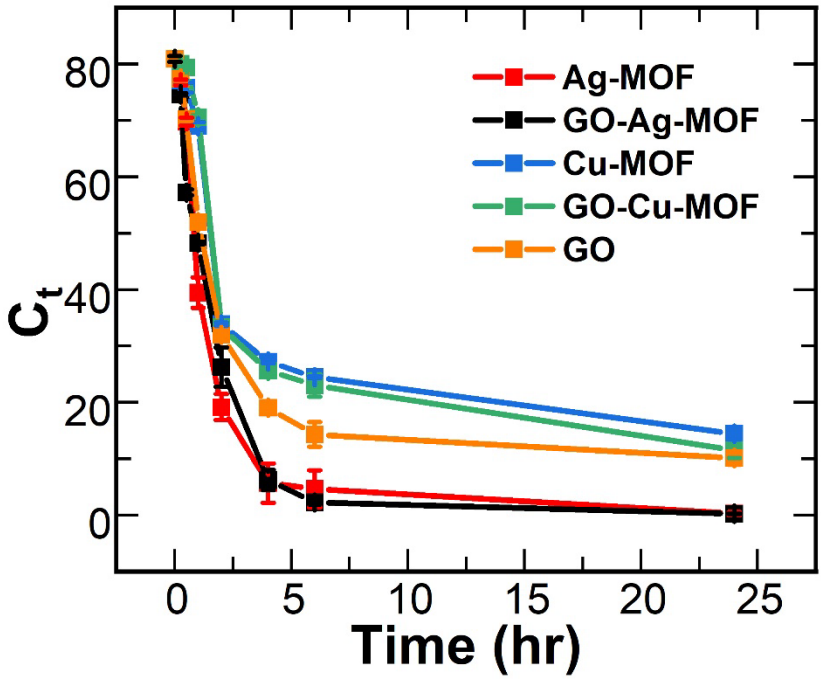

Figure S5. Kinetic experiments on Cu-MOF, GO-Cu-MOF, Ag-MOF, GO-Ag-MOF and GO are carried out for 24 hrs. The initial concentration of dye was 70 ppm. C_t is the transient concentration at time t.

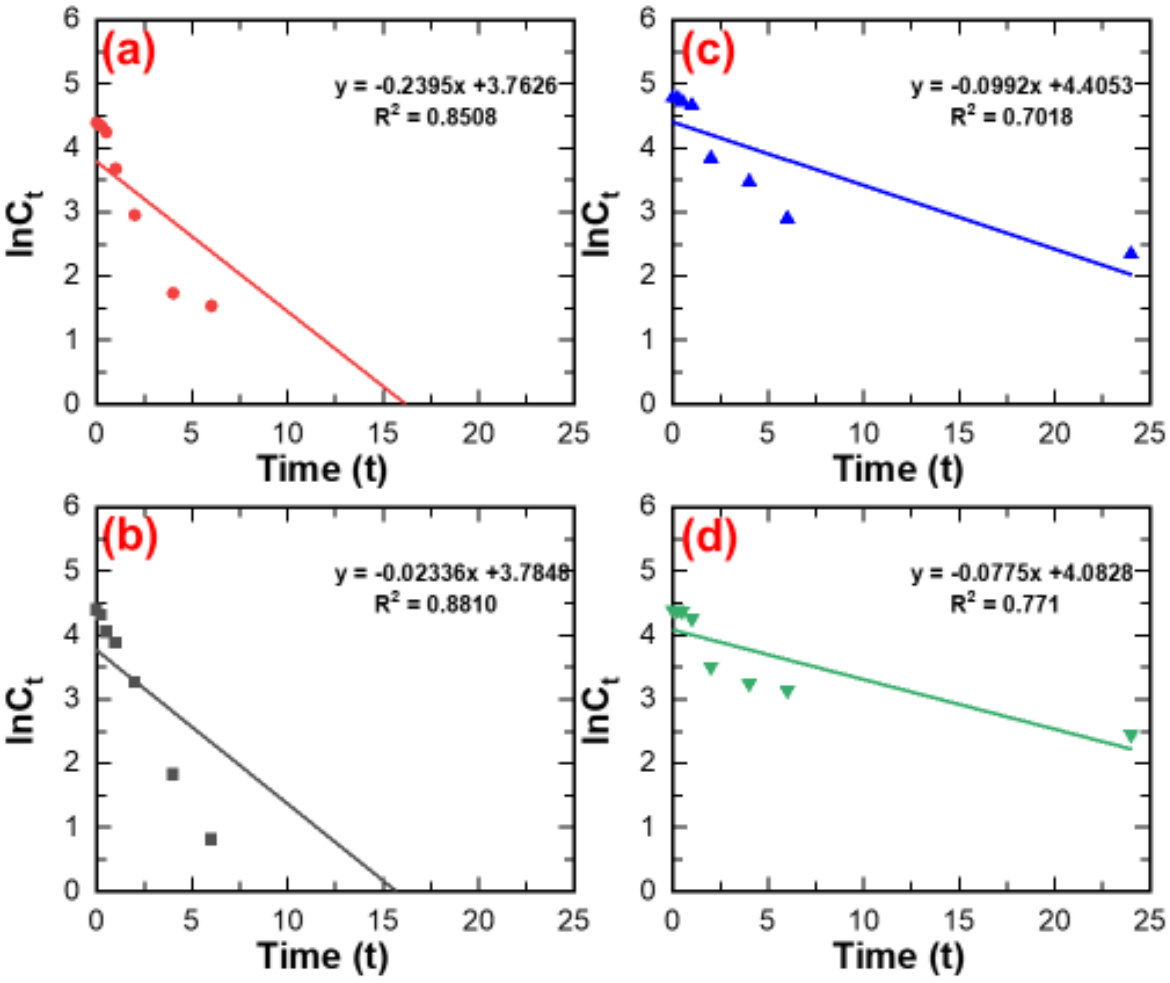

Figure S6. Psuedo first order model fitting on Cu-MOF, GO-Cu-MOF, Ag-MOF, GO-Ag-MOF and GO are carried out for 24 hrs. The initial concentration of dye was 70 ppm. C_t is the transient concentration at time t.